

## MONITORING AGNS WITH H $\beta$ ASYMMETRY. I. FIRST RESULTS: VELOCITY-RESOLVED REVERBERATION MAPPING

PU DU,<sup>1</sup> MICHAEL S. BROTHERTON,<sup>2</sup> KAI WANG,<sup>1</sup> ZHENG-PENG HUANG,<sup>1</sup> CHEN HU,<sup>1</sup> DAVID H. KASPER,<sup>2</sup> WILLIAM T. CHICK,<sup>2</sup>  
MY L. NGUYEN,<sup>2</sup> JAYA MAITHIL,<sup>2</sup> DEREK HAND,<sup>2</sup> YAN-RONG LI,<sup>1</sup> LUIS C. HO,<sup>3,4</sup> JIN-MING BAI,<sup>5</sup> WEI-HAO BIAN,<sup>6</sup> AND  
JIAN-MIN WANG<sup>1,7,8,\*</sup>  
(MAHA COLLABORATION)

<sup>1</sup>Key Laboratory for Particle Astrophysics, Institute of High Energy Physics, Chinese Academy of Sciences, 19B Yuquan Road, Beijing 100049, China;  
*dupu@ihep.ac.cn, wangjm@ihep.ac.cn*

<sup>2</sup>Department of Physics and Astronomy, University of Wyoming, Laramie, WY 82071, USA; *mbrother@uwyo.edu*

<sup>3</sup>Kavli Institute for Astronomy and Astrophysics, Peking University, Beijing 100871, China

<sup>4</sup>Department of Astronomy, School of Physics, Peking University, Beijing 100871, China

<sup>5</sup>Yunnan Observatories, Chinese Academy of Sciences, Kunming 650011, China

<sup>6</sup>Physics Department, Nanjing Normal University, Nanjing 210097, China

<sup>7</sup>National Astronomical Observatories of China, Chinese Academy of Sciences, 20A Datun Road, Beijing 100020, China

<sup>8</sup>School of Astronomy and Space Science, University of Chinese Academy of Sciences, 19A Yuquan Road, Beijing 100049, China

### ABSTRACT

We have started a long-term reverberation mapping project using the Wyoming Infrared Observatory 2.3 meter telescope titled “Monitoring AGNs with H $\beta$  Asymmetry” (MAHA). The motivations of the project are to explore the geometry and kinematics of the gas responsible for complex H $\beta$  emission-line profiles, ideally leading to an understanding of the structures and origins of the broad-line region (BLR). Furthermore, such a project provides the opportunity to search for evidence of close binary supermassive black holes. We describe MAHA and report initial results from our first campaign, from December 2016 to May 2017, highlighting velocity-resolved time lags for four AGNs with asymmetric H $\beta$  lines. We find that 3C 120, Ark 120, and Mrk 6 display complex features different from the simple signatures expected for pure outflow, inflow, or a Keplerian disk. While three of the objects have been previously reverberation mapped, including velocity-resolved time lags in the cases of 3C 120 and Mrk 6, we report a time lag and corresponding black hole mass measurement for SBS 1518+593 for the first time. Furthermore, SBS 1518+593, the least asymmetric of the four, does show velocity-resolved time lags characteristic of a Keplerian disk or virialized motion more generally. Also, the velocity-resolved time lags of 3C 120 have significantly changed since previously observed, indicating an evolution of its BLR structure. Future analyses of the data for these objects and others in MAHA will explore the full diversity of H $\beta$  lines and the physics of AGN BLRs.

*Keywords:* galaxies: active; galaxies: nuclei - quasars: supermassive black holes

### 1. INTRODUCTION

The most prominent features in the UV and optical spectra of luminous active galactic nuclei (AGNs) and quasars are the broad emission lines (BELs), with velocity widths ranging from  $\sim 10^3$  km s<sup>-1</sup> to  $\sim 10^4$  km s<sup>-1</sup> (e.g., Schmidt 1963; Osterbrock & Mathews 1986; Boroson & Green 1992; Sulentic et al. 2000; Shen et al. 2011, and references therein). The spectra generally show similarities from local Seyfert galaxies all the way to  $z \gtrsim 7$  quasars (e.g., Francis & Koratkar 1995; Vanden Berk et al. 2001; Mortlock et al. 2011; Bañados et al. 2018). This suggests that the broad-line regions (BLRs) of AGNs have similarities from object to object over cosmological time. The similarities lead to recogni-

tion of a common formation mechanism of the BLRs in most AGNs and quasars, and also to the importance of investigating nearby AGNs for insight into high- $z$  quasars. However, we so far possess insufficient understanding of the BLRs and their physics.

Reverberation mapping (RM) campaigns (e.g., Peterson et al. 1993, 1998, 2002, 2004; Kaspi et al. 2000, 2007; Bentz et al. 2008, 2009; Denney et al. 2009; Barth et al. 2011, 2013, 2015; Rafter et al. 2011, 2013; Du et al. 2014, 2015, 2016b, 2018; Wang et al. 2014; Shen et al. 2016b; Fausnaugh et al. 2017; Grier et al. 2012, 2017b) provide measurements of BEL lags ( $\tau_{\text{BLR}}$ ) with respect to the varying ionizing continuum as originally suggested by Bahcall et al. (1972) and Blandford & McKee (1982). The time lag multiplied by the speed of light ( $c$ ) provides the size scale of the BLR. In individual objects, different lines echoing at different distances

\* PI of the MAHA Project

are consistent with the same virial black hole mass

$$M_{\bullet} = f_{\text{BLR}} \frac{R_{\text{BLR}} \Delta V^2}{G}, \quad (1)$$

indicating Keplerian motion, where  $G$  is the gravitational constant,  $R_{\text{BLR}} = c\tau_{\text{BLR}}$  is the emissivity-weighted radius of the BLR,  $\Delta V$  is either full-width-half-maximum (FWHM) or velocity dispersion ( $\sigma_{\text{line}}$ ) of mean spectra or root-mean-square (rms) spectra (Peterson & Wandel 1999; Wandel et al. 1999), and  $f_{\text{BLR}}$  is the virial factor determined by the geometry and kinematics of the BLR (e.g., Peterson et al. 2004). In past decades, RM established a tight correlation between time lags and luminosity based on a heterogeneous AGN sample containing mostly sub-Eddington sources (Kaspi et al. 2000; Bentz et al. 2013). More recently, however, new RM campaigns have discovered that lags are substantially shorter for super-Eddington AGNs than their sub-Eddington counterparts of the same luminosity (Du et al. 2015, 2016b, 2018). Beyond just determining a single global time lag, high-quality reverberation mapping can provide time lags as a function of velocity. Such velocity-resolved time lags are diagnostic of the BLR structure itself, and these and other advanced analysis products such as velocity-delay maps and dynamical models commonly find that the BLR is comprised of a thick Keplerian disk (e.g., Bentz et al. 2008; Denney et al. 2010; Grier et al. 2013b; Pancoast et al. 2014; Du et al. 2016a; Grier et al. 2017a)<sup>1</sup>. This flattened disk of BLRs as the major ingredient could be common in AGNs and quasars. The BLR, however, appears significantly more complex in many objects.

The BEL profiles (especially those of the  $\text{H}\beta$  line) of most AGNs are roughly symmetric (e.g., Gaussian or Lorentzian-like), but there are still a large number of objects showing asymmetric (redward, blueward or even double-peaked) profiles both for low and high-ionization lines (e.g., Boroson & Green 1992; Eracleous & Halpern 1994; Brotherton 1996; Peterson 1997). Similarly,  $\text{H}\beta$  usually shows a line peak close to systemic velocity, but extreme outliers exist (Eracleous et al. 2012; Shen et al. 2016a). Some net radial motion and/or opacity effects would seem required to explain BLRs displaying extreme profiles. The BELs with the extreme profiles may indicate special geometry and kinematics of their BLRs, such as super-fast or ultra-strong inflow or outflow, or even abnormal nuclear environments (e.g., absorption or dust). The asymmetries of  $\text{H}\beta$  profiles significantly correlate with the ratio of Fe II to  $\text{H}\beta$  (Boroson & Green 1992), and with [O III] luminosities (Wang et al. 2017a). High-precision RM has shown indications of infall and (more rarely) outflow

<sup>1</sup> There are several other lines of evidence indicate that the typical BLR has the structure and dynamics of a flattened disk with emission-line gas following Keplerian motion (see Gaskell 2009 for a review of the BLR). For instance,  $\text{H}\beta$  velocity widths are systematically smaller in more face-on systems as determined using orientation-dependent radio properties (Wills & Browne 1986), and spectropolarimetry of type 1 AGNs also supports a flattened, disk-like geometry (Smith et al. 2005; Baldi et al. 2016; Savić et al. 2018).

**Table 1.** Featured Targets

Object	$\alpha_{2000}$	$\delta_{2000}$	Redshift	$N_{\text{spec}}$	Cadence
3C 120	04 33 11.1	+05 21 16	0.0330	27	3.6
Ark 120	05 16 11.4	−00 08 59	0.0327	22	4.3
Mrk 6	06 52 12.2	+74 25 37	0.0188	45	3.4
SBS 1518+593	15 19 21.6	+59 08 24	0.0781	20	6.8

NOTE— $N_{\text{spec}}$  is the number of spectroscopic epochs. “Cadence” is the average sampling interval of the objects in days.

in  $\text{H}\beta$ -emitting gas, sometimes in the presence of a Keplerian disk component as well (e.g., Grier et al. 2017a). Some objects with excellent RM data sets have defied simple explanation, such as Mrk 6 (Doroshenko et al. 2012; Grier et al. 2013b). Mrk 6 is also noteworthy for its complex  $\text{H}\beta$  profile, which possesses a strongly blueshifted peak in addition to a lower velocity peak in most epochs, and red asymmetric tail. More detailed investigations of such AGNs are needed to provide a deeper understanding of the full diversity of the structure and kinematics of the BLR, and perhaps clues to its origin as well. The latter has been a controversial subject that is not yet resolved, although there are many proposals (Murray & Chiang 1997; Czerny & Hryniewicz 2011; Elvis 2017; Wang et al. 2017a; Baskin & Laor 2018).

Another intriguing hypothesis to explain some asymmetric and shifted profiles is the existence of close binary supermassive black holes (CB-SMBHs) in AGNs. CB-SMBHs have been predicted to be located in galactic centers due to galaxy mergers (Begelman et al. 1980), however, one single black hole is commonly assumed in explanations of RM data. This assumption may be challenged by the more unusual profiles of BELs implying the potential presence of CB-SMBHs (e.g., Gaskell 1996; Eracleous et al. 1997, 2012; Boroson & Lauer 2009; Bon et al. 2012, 2016; Li et al. 2016, 2017; Decarli et al. 2013; Shen et al. 2013; Wang et al. 2017b; Runnoe et al. 2017; Nguyen & Bogdanović 2016; Pflueger et al. 2018), which could be an indicator of CB-SMBHs (Popovic et al. 2000; Shen & Loeb 2010). However, there are several alternative explanations for the complicated profiles, such as elliptical BLR disks for asymmetric or double-peaked profiles (Eracleous et al. 1997), hot spots (Jovanović et al. 2010), partially covering dusty obscurers (Gaskell & Harrington 2018), and even spiral-arms (Storchi-Bergmann et al. 2017). Recoiling AGNs may be an additional possibility if the velocity is high enough to create an appreciable shift from a narrow-line region reflecting the redshift of the host galaxy (Volonteri & Madau 2008).

CB-SMBHs are expected to be sources of nano-Hz gravitational waves, likely to be discovered by Pulsar Timing Arrays (e.g., Sesana et al. 2008). While it is likely impossible to convincingly diagnose the presence of CB-SMBHs using single epoch spectra, time-series spectroscopy of BELs may prove successful. Recently, Wang et al. (2018) suggested a high-fidelity RM campaign to determine velocity delay maps

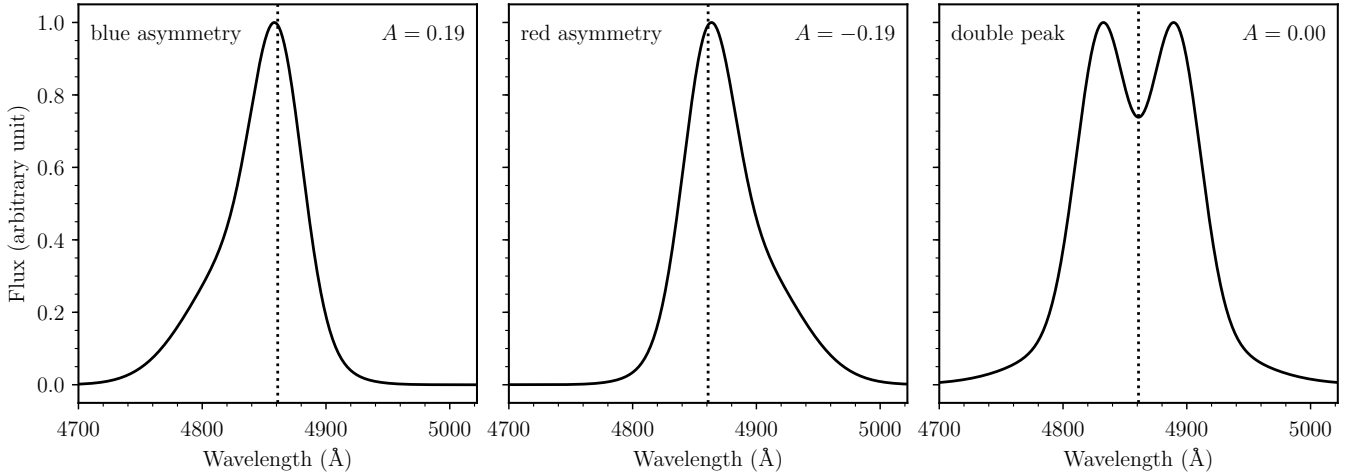


**Figure 1.** Schematic diagram for asymmetric and double-peaked profiles.  $A$  is defined as Equation 2. The dotted lines mark  $4861\text{\AA}$ .

for AGNs that are binary candidates in order to provide the optical identification of CB-SMBHs.

For these reasons, we have undertaken the “Monitoring AGNs with  $H\beta$  Asymmetry” (MAHA) project. We describe our target selection, observations, and data reduction in Section 2. We report the initial results for four AGNs here, specifically: the mean and rms spectra in Section 2.3; the measurement of the light curves in Section 3; the lag measurements, the widths of the  $H\beta$  lines, black hole masses, and the velocity-resolved time lags in Section 4. We discuss the results for each individual object in Section 5. Finally, we summarize our findings in Section 6.

## 2. MAHA: TARGETS, OBSERVATIONS, DATA REDUCTION

Below we describe our MAHA target selection as well as our program of observations and data reduction that we started in December 2016. Due to a lack of significant variability, long time lags comparable to the length of an individual seasonal campaign, or other issues, many objects will require multiple campaigns to produce high-quality results of the type we seek. We expect to add or drop objects as MAHA progresses for a variety of reasons, so the sample should not be considered as absolute. The sample should, however, illustrate the type of objects we are monitoring and the diversity of their  $H\beta$  profiles. Our observational methods and data reduction apply generally to the entire sample, although we provide measurements and analyses in this first paper for only four objects for which we have obtained good quality velocity-resolved time lags.

### 2.1. Targets

The core MAHA sample includes AGNs with asymmetric or double-peaked  $H\beta$  emission lines, as well as objects reported as binary black hole candidates (which usually also have asymmetric lines). While the majority of the  $H\beta$  profiles of MAHA targets can easily be visually identified as asymmetric, it will be useful to parameterize asymmetry. There exist many ways to quantify asymmetry, each with its

pros and cons. For ease of historical comparison to previous work (e.g., De Robertis 1985; Boroson & Green 1992; Brotherton 1996), we adopt the dimensionless asymmetry parameter:

$$A = \frac{\lambda_c(3/4) - \lambda_c(1/4)}{\Delta\lambda(1/2)} \quad (2)$$

where  $\lambda_c(3/4)$  and  $\lambda_c(1/4)$  are the central wavelengths at the 3/4 and 1/4 of the peak height, and  $\Delta\lambda(1/2)$  is the FWHM. Blue asymmetries are positive, red are negative. Note that the asymmetry is independent of any peak or centroid wavelength shift relative to systemic. Figure 1 illustrates what we mean when we say red and blue asymmetries and double-peaked lines.

We selected our targets from a variety of literature sources based on both asymmetry measurements and visual inspection of optical spectra (e.g., De Robertis 1985; Stirpe 1990; Boroson & Green 1992; Eracleous & Halpern 1993, 1994; Marziani et al. 2003; Hu et al. 2008a,b; Eracleous et al. 2012). We selected some additional sources directly from the quasar sample of the Sloan Digital Sky Survey (SDSS) (Schneider et al. 2010), decomposing the  $H\beta$  lines by two Gaussians through the multi-component fitting procedure in Hu et al. (2008a,b), then selecting objects for which the two Gaussians have substantially different central velocities. This method recovered many objects already identified from the literature sources above.

Using the Wyoming Infrared Observatory (WIRO) 2.3 meter telescope and its longslit spectrograph requires additional selection criteria. WIRO has a latitude of  $41^\circ$  N, and we do not include targets south of declination  $\sim -10^\circ$ . In order to obtain sufficiently high signal-to-noise ratios (S/N) in exposure times of  $\sim 1$  hour or less, the magnitude (in V or SDSS  $r'$  band) needs to be brighter than  $\sim 17$ . We also require  $z < 0.38$  to keep  $[\text{O III}]\lambda 5007$  at less than  $7000\text{\AA}$  observed frame to avoid the inefficiencies of grating tilts and extra calibrations. Finally, because of our procedure for photometric calibration using narrow lines,  $[\text{O III}]\lambda 5007$  cannot be too weak. When

**Table 2.** Measurement windows in the observed-frame and [O III] standard fluxes

Object	$F_{[\text{O III}]}$ ( $10^{-13}$ erg s $^{-1}$ cm $^{-2}$ )	[O III]			H $\beta$		
		continuum (blue)	line	continuum (red)	continuum (blue)	line	continuum (red)
		( $\text{\AA}$ )					
3C 120	3.07	5140–5150	5150–5200	5200–5215	4943–4965	4965–5060	5088–5103
Ark 120	0.84	5140–5150	5150–5195	5195–5210	4927–4950	4950–5138	5196–5215
Mrk 6	6.32	5070–5080	5080–5130	5130–5150	4820–4850	4850–5076	5138–5168
SBS 1518+593	0.44	5365–5375	5375–5420	5420–5435	5175–5196	5200–5300	5315–5331

everything else is equal, we prefer brighter targets at lower redshifts and more northern declinations.

We do not automatically exclude AGNs from MAHA just because they have previous RM results. BLRs and their corresponding H $\beta$  asymmetries may evolve over time periods of several years. Additionally, we aim to obtain high enough data quality to not only determine velocity-resolved time lags, but also to conduct more involved analyses such as creating velocity-delay maps and dynamical models (e.g., Horne 1994; Horne et al. 2004; Bentz et al. 2010; Grier et al. 2013b; Skielboe et al. 2015; Pancoast et al. 2011, 2012, 2014; Grier et al. 2017a).

We provide additional information about the MAHA targets and their spectra in Appendix A, including the initial MAHA sample, its characteristics, and example WIRO spectra of the H $\beta$  line region obtained during 2016–2018. Because of the need to use [O III] to calibrate fluxes in WIRO spectra, and the fact that objects with strong [O III] tend to be the ones with the strongest red asymmetric H $\beta$  lines (Boroson & Green 1992), our sample is biased against objects with blue asymmetric H $\beta$  lines. We plan to search for and add more AGNs with blue asymmetric H $\beta$  lines as MAHA progresses.

As the first paper of the series, we provide here our RM measurements of 4 AGNs: 3C 120, Ark 120, Mrk 6, and SBS 1518+593 (see Table 1 for their coordinates and some general information). Their luminosities place them among Seyfert galaxies and broad line radio galaxies rather than the more energetic quasar category. Ark 120 and Mrk 6 show extreme red asymmetric profiles, while 3C 120 and SBS 1518+593 show milder red asymmetries. None are extreme super-Eddington accretors, although 3C 120 and SBS 1518+593 have dimensionless accretion rates  $\dot{M}$  on order unity (Du et al. 2015, see also 4.3). The light curves of all these sources have shown unambiguous peaks or dips, and are sufficient for us to measure H $\beta$  time lags.

## 2.2. Observations

### 2.2.1. Spectroscopy

We obtained spectroscopic data using the 2.3 m telescope at the WIRO and its Long Slit Spectrograph, observing remotely from the University of Wyoming campus (Findlay et al. 2016). We used the 900 line mm $^{-1}$  grating, which pro-

vides a dispersion of 1.49  $\text{\AA}$  pixel $^{-1}$  and a wavelength coverage of 4000 – 7000  $\text{\AA}$ . We adopted a slit width of 5'' in order to minimize the light losses due to the aperture effect. We reduced the spectra with IRAF v2.16, and extracted them using a uniform aperture of  $\pm 6''.8$  and background windows of  $7''.6 - 15''.1$  on both sides. The wavelengths of the spectra are calibrated by taking CuAr lamp exposures. For each object, we took several consecutive exposures in order to estimate the systematic flux calibration uncertainties (see Section 2.2.2).

### 2.2.2. Spectrophotometry

We initially flux calibrated the spectra using one or more spectrophotometric standard stars observed each night (primarily Feige 34, G191B2B, or BD+28d4211). However, due to variable atmospheric extinction during the night, we took additional measures to obtain accurate photometry. We used established techniques to use [O III] lines for flux calibration (van Groningen & Wanders 1992; Fausnaugh 2017), which ensures good accuracy even in relatively poor observing conditions. The variable time scales of the [O III]  $\lambda 5007$  lines are much longer than one year for luminous AGNs as they originate from much more extended narrow-line regions (Peterson et al. 2013). Therefore, [O III] lines can be used as flux standards to calibrate the spectra.

We used a 5''-wide slit, which is wider than the FWHM of the seeing ( $2'' \sim 3''$ ) during all of the observations. The variable seeing at different times leads to the change of the line spread function (spectral resolution, see more details in Du et al. 2016a). Additionally, the tracking inaccuracy of the telescope sometimes made the line spread function deviate from a Gaussian. Thus, before scaling the spectra according to their [O III] fluxes, we convolved the [O III] profiles of the spectra by a double-Gaussian (a sum of two Gaussians) function ( $\zeta$ )<sup>2</sup> that fit the broadest [O III] profile for each object (a Gaussian with the same FWHM as the broadest [O III] was used instead if the broadest [O III] itself significantly differed from Gaussian). We extracted the [O III] profiles by subtracting the local continuum underneath determined by interpola-

<sup>2</sup>  $\zeta$  is not the line spread function. It represents the differences between the spectral broadening of the spectrum and the broadest spectral broadening function of the object.

tion between two nearby background windows. We provide the extraction and local continuum windows in Table 2. The optimal parameters of  $\zeta$  were determined by the Levenberg-Marquardt algorithm. Then, all of the spectra were smoothed by convolution with their corresponding  $\zeta$  to minimize the influence due to the variable seeing and the tracking inaccuracies. It should be noted that the spectral resolution after the convolution is lower than that of the original spectrum, but still quite sufficient to resolve broad H $\beta$  profiles.

After that, each exposure of the object was scaled to match its standard [O III] flux. The [O III] fluxes were measured using the windows listed in Table 2, and the standard [O III] fluxes (listed in Table 2) of the objects are determined by the spectra taken in the photometric conditions. We produced the final calibrated spectra by averaging the (appropriately noise-weighted) exposures in the same night for each object.

### 2.3. Mean and RMS spectra

To demonstrate the spectral characteristics and to evaluate the variation amplitude at different wavelengths, we plot the mean and root-mean-square (rms) spectra for each object in Figure 2. The mean and rms spectra are defined as

$$\bar{F}_\lambda = \frac{1}{N} \sum_{i=1}^N F_\lambda^i \quad (3)$$

and

$$S_\lambda = \left[ \frac{1}{N} \sum_{i=1}^N (F_\lambda^i - \bar{F}_\lambda)^2 \right]^{1/2}, \quad (4)$$

respectively.  $F_\lambda^i$  is the  $i$ -th spectrum, and  $N$  is the number of spectra for this object. The [O III] and the narrow H $\beta$  emission lines in the rms spectra are extremely weak, which indicates that the calibration procedure in Section 2.2.2 works very well. The obvious broad H $\beta$  lines in the rms spectra imply that their variations are significant.

## 3. LIGHT CURVES

### 3.1. Light curves from WIRO

The fluxes of the H $\beta$  emission line can be measured by direct integration (e.g., Peterson et al. 1998; Kaspi et al. 2000; Bentz et al. 2009; Grier et al. 2012; Du et al. 2014; Fausnaugh et al. 2017) or by spectral fitting (e.g., Barth et al. 2013; Hu et al. 2015). The first method measures the flux by integrating the H $\beta$  line after subtracting the local background determined by two continuum windows. The second method separates the emission lines from the continuum by multi-component spectral fitting, and has been gradually adopted in recent years. Considering that (1) it is difficult to fit the very complex and asymmetric H $\beta$  profiles of our targets perfectly by multiple Gaussian or Lorentzian functions, or their combinations; (2) the integration method is more robust and works well for isolated emission line like H $\beta$ , we choose to use the integration method to measure the H $\beta$  light curves in this work.

We chose the windows for H $\beta$  flux measurements that cover the H $\beta$  emission shown in their rms spectra (Figure 2) and avoid the possible influences from their [O III] lines. The local continuum windows were selected as minimally variable regions in the rms spectra. We provide the line and the local continuum windows of H $\beta$  in Table 2 and show them in Figure 2. We measured the H $\beta$  light curves by integrating the fluxes in the H $\beta$  windows after subtracting the local continuum determined by interpolating between the two nearby continuum windows. Similar to the narrow [O III] lines, the flux of the narrow H $\beta$  can be regarded as a constant during our campaign. Thus, we did not remove the contributions of the narrow H $\beta$  lines from the measured H $\beta$  light curves. We obtained the 5100Å continuum light curves by averaging the fluxes from 5075 to 5125Å in the rest-frames (shown as grey regions in Figure 2).

The error bars of the fluxes in the light curves include two components: (1) the Poisson noise and (2) the systematic uncertainties. The systematic uncertainties result primarily from the variable atmospheric extinction (especially in poor weather conditions) and telescope-tracking inaccuracies, and we estimated them using the scatter of the mean fluxes of the exposures in the same night over a wider range of wavelength ( $\sim 4700$ – $5100$ Å). The two components summed in quadrature provide the error bars of the points in the light curves (see Figure 3). However, the above error bars likely do not account for all of the systematic uncertainties for most of the objects (the flux differences between adjacent nights are sometimes larger than the error bars and unlikely to result solely from real variability). We show additional systematic uncertainties estimated by the median filter method (see more details in Du et al. 2014), which smooths the light curve by a median filter of 5 points and then obtains the systematic uncertainty from the standard deviation of the residuals after subtracting the smoothed light curve, if necessary, as the gray error bars in the lower-right corners in Figure 3<sup>3</sup>. These are also taken into account in the following time-series analysis (Section 4.1) by added in quadrature to the error bar of every data point in Figure 3. We provide the 5100 Å and H $\beta$  light curves in Figure 3 and Table 3.

### 3.2. Photometric light curves from ASAS-SN

Photometric observations based on imaging are commonly carried out simultaneously with the spectroscopic observations in many RM campaigns (e.g., Bentz et al. 2009; Denney et al. 2010; Du et al. 2014, 2015, 2016b, 2018; Wang et al. 2014; Fausnaugh et al. 2017). The photometric light curves can be used to check the calibration precision of the spectroscopic observations, and furthermore can be adopted as sup-

<sup>3</sup> The systematic uncertainties obtained by the median filter (the gray error bars in the corners of Figure 3) are 0.10 and 0.05, 0.07 and 0.13, and 0.05 and 0.04 for the continuum and emission-line light curves of 3C 120, Ark 120, and Mrk 6, respectively. The units are  $10^{-15}$  erg s $^{-1}$  cm $^{-2}$  Å $^{-1}$  and  $10^{-13}$  erg s $^{-1}$  cm $^{-2}$  for the continuum and emission-line fluxes. For SBS 1518+593, the extra systematic uncertainties are not necessary. The original error bars are already large enough.

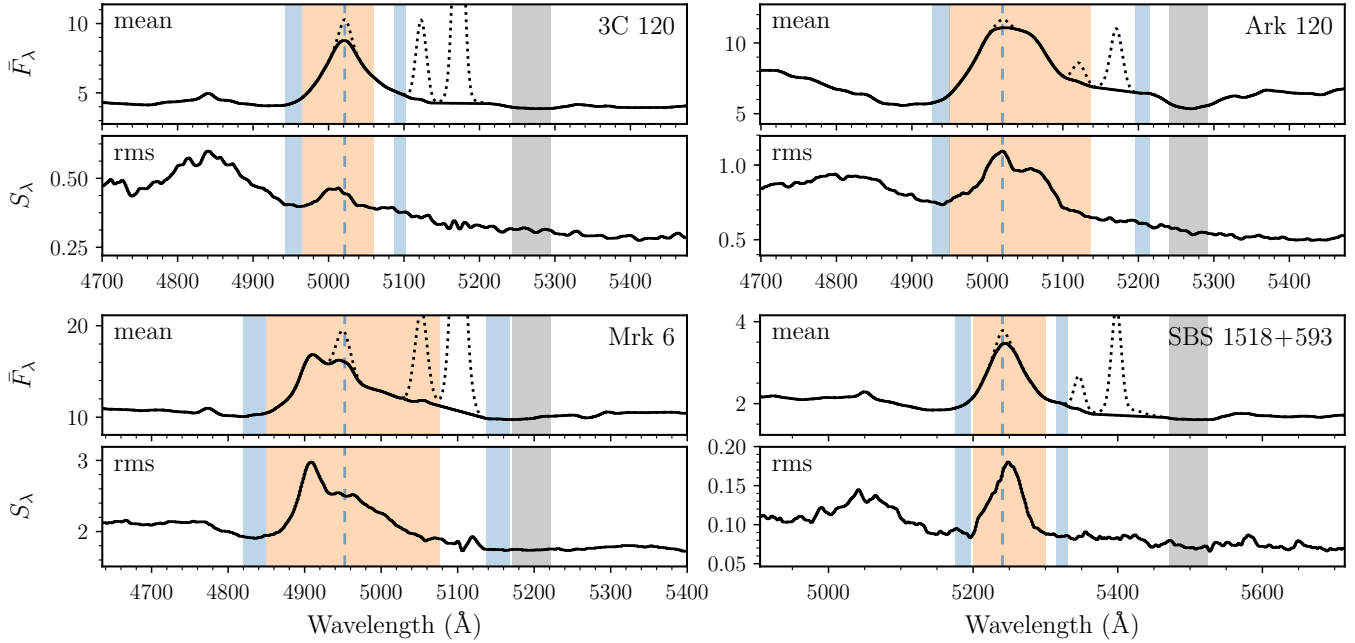


**Figure 2.** Mean and rms spectra in the observed-frame of the objects. The solid lines are the narrow-line-subtracted mean and rms spectra, and the dotted lines are the narrow H $\beta$  and [O III] $\lambda$ 4959, 5007 (see more details in Section 4.2). The orange and blue regions are the windows for H $\beta$  emission lines and their backgrounds. The gray regions mark the 5100Å continuum windows. We plot  $4861 \times (1+z)$  Å as blue dashed lines in order to illustrate their asymmetric H $\beta$  profiles more clearly. The flux density units are  $10^{-15}$  erg s $^{-1}$  cm $^{-2}$  Å $^{-1}$ .

**Table 3.** Light curves

3C 120			Ark 120		
JD	$F_{5100}$	$F_{H\beta}$	JD	$F_{5100}$	$F_{H\beta}$
52.65	$4.00 \pm 0.02$	$2.48 \pm 0.01$	43.71	$5.28 \pm 0.09$	$5.66 \pm 0.09$
71.64	$3.98 \pm 0.01$	$2.55 \pm 0.01$	52.68	$5.41 \pm 0.03$	$5.39 \pm 0.02$
72.59	$3.98 \pm 0.02$	$2.49 \pm 0.02$	53.68	$5.52 \pm 0.09$	$5.48 \pm 0.09$
74.70	$4.06 \pm 0.01$	$2.53 \pm 0.01$	71.65	$6.07 \pm 0.09$	$5.54 \pm 0.08$
80.58	$4.14 \pm 0.02$	$2.51 \pm 0.01$	72.61	$6.26 \pm 0.14$	$5.59 \pm 0.12$

NOTE—JD: Julian dates from 2,457,700;  $F_{5100}$  and  $F_{H\beta}$  are the continuum fluxes at 5100 Å and H $\beta$  fluxes in units of  $10^{-15}$  erg s $^{-1}$  cm $^{-2}$  Å $^{-1}$  and  $10^{-13}$  erg s $^{-1}$  cm $^{-2}$ , respectively. This table is available in its entirety in a machine-readable form in the online journal. A portion is shown here for guidance regarding its form and content.

plemental to the 5100Å light curves, especially if the sampling of the spectroscopic observations is relatively poor or their monitoring period is not long enough. We did not conduct our own photometric observations during 2016–2017 in our campaign. However, because the objects of this paper are bright enough, we can find their photometric light curves from archival data from the All-Sky Automated Survey for Supernovae (ASAS-SN)<sup>4</sup>. ASAS-SN is a long-term project useful to discover and study supernovae, transients,

<sup>4</sup> <http://www.astronomy.ohio-state.edu/~assassin/index.shtml>

and other variable sources by automatic and regular sky survey, and provides photometric light curves for the objects down to  $\sim 17$  magnitude. More information and technical details about the ASAS-SN light curves are provided by, e.g., Shappee et al. (2014) and Kochanek et al. (2017). Figure 3 shows the scaled ASAS-SN light curves of our targets (more details of the scaling are provided in Section 3.3). We removed several points with very poor S/N. The variations of the 5100Å and the ASAS-SN light curves are consistent (see Figure 3), thus it verifies our spectroscopic calibration.

### 3.3. Combined continuum light curves

Considering that the ASAS-SN observations can extend the temporal spans of our continuum light curves and improve their sampling cadences, we averaged the ASAS-SN and the 5100Å light curves to produce a combined continuum light curve for each object. Because of differing apertures (ASAS-SN uses an aperture with a radius of  $15''.6$ ), the ASAS-SN light curves require adjustment to match the mean fluxes and the variation amplitudes of the WIRO 5100Å light curves before combination. This was performed by assuming

$$F_{5100} = a + b \times F_{\text{ASAS-SN}}, \quad (5)$$

where  $F_{5100}$  and  $F_{\text{ASAS-SN}}$  are the 5100Å and ASAS-SN fluxes of the closely adjacent pairs of the observations (the separation is at most less than 2 days),  $a$  is a flux adjustment, and  $b$  is a scale factor. We determined the values of  $a$  and  $b$  by using the FITEXY algorithm (Press et al. 1992). Then, we scaled the ASAS-SN light curves by applying Equation

**Table 4.** Time lags

Object	Continuum	$r_{\max}$	Observed	Rest-frame	Note	
			Time Lag	Time Lag		
			(days)	(days)		
3C 120	5100Å	0.76	$20.9^{+5.1}_{-4.4}$	$20.2^{+5.0}_{-4.2}$	✓	
	combined	0.71	$19.3^{+3.0}_{-3.0}$	$18.7^{+2.9}_{-2.9}$		
Ark 120	5100Å	0.94	$16.7^{+3.3}_{-3.2}$	$16.2^{+3.2}_{-3.1}$	✓	
	combined	0.83	$13.8^{+3.1}_{-2.8}$	$13.4^{+3.0}_{-2.7}$		
Mrk 6	5100Å	0.99	$40.4^{+5.2}_{-11.4}$	$39.6^{+5.1}_{-11.2}$	✓	
	combined	0.99	$18.8^{+2.5}_{-2.5}$	$18.5^{+2.5}_{-2.4}$		
SBS 1518+593	5100Å	0.93	$21.2^{+10.7}_{-6.4}$	$19.7^{+9.9}_{-6.0}$	✓	
	combined	0.88	$30.6^{+8.9}_{-7.3}$	$28.4^{+8.3}_{-6.8}$		

NOTE—“✓” means we use this time lag of the object to calculate its black hole mass in Table 6.

(5), and combined the 5100Å and ASAS-SN light curves by weighted averaging all of the observations in the same nights. The uncertainties of the weighted mean<sup>5</sup> are simply adopted as the error bars in the combined light curves. We tried to use the median filter method to estimate the systematic uncertainties, and found no extra systematic uncertainties are needed for the combined light curves. Figure 3 shows both the scaled ASAS-SN light curves and the final combined light curves.

## 4. ANALYSIS

### 4.1. Cross-correlation function

The time delays between the variations of the continuum and H $\beta$  emission lines were determined by using the interpolated cross-correlation function (ICCF; Gaskell & Sparke 1986; Gaskell & Peterson 1987). To measure the time delay we used the centroid of the ICCF above 80% of the peak (a typical value used in many RM investigations, e.g., Bentz et al. 2009; Du et al. 2014; Fausnaugh et al. 2017).

We estimated the uncertainties of the time delays through the “flux randomization/random subset sampling (FR/RSS)” method (Peterson et al. 1998, 2004). The procedure takes into account both the measurement errors of the fluxes and the uncertainties due to the sampling/cadence. This method generates light curve realizations by perturbing the fluxes in accordance with their error bars and randomly sub-sampling the data points in the light curves. The cross-correlation centroid distributions (CCCDs) are obtained by performing the ICCF to the light curve realizations. The median and the 68% confidence intervals of the CCCDs are adopted as the final time lags and their uncertainties. The auto-correlation functions (ACFs), the CCFs, and the CCCDs of the 5100Å and H $\beta$  light curves for each object are shown in Figure 3. Table 4 gives The time lag measurements and the correspond-

<sup>5</sup> The uncertainties of the weighted mean is defined as  $\sigma_{\text{mean}} = (1/\sum \sigma_i^{-2})^{1/2}$ , where  $\sigma_i$  is the uncertainty of each point in the same night.

**Table 5.** Narrow-line flux ratios

Object	[O III] $\lambda$ 5007/[O III] $\lambda$ 4959	[O III] $\lambda$ 5007/H $\beta$
3C 120	$3.06 \pm 0.04$	$11.16 \pm 0.40$
Ark 120	$3.20 \pm 0.07$	$8.65 \pm 0.46$
Mrk 6	$3.15 \pm 0.05$	$9.19 \pm 0.31$
SBS 1518+593	$3.18 \pm 0.04$	$7.74 \pm 0.29$

ing maximum correlation coefficients of the CCFs. We also measured the H $\beta$  time delays relative to the combined continuum light curves (see Section 3.3), and provide the results in Figure 3 and in Table 4.

Although the photometric data can in principle extend the temporal spans of the 5100Å light curves and improve the sampling cadences, the scatter of the ASAS-SN light curves are generally larger than that of the 5100Å light curves in our campaign because of the limited collecting area of the ASAS-SN telescopes. We used the lag measurements of the combined continuum versus the H $\beta$  light curves only in the case of Mrk 6, which greatly extended continuum coverage and resulted in a clearly improved result. The H $\beta$  time lags we used in the following analysis are labeled by “✓” in Table 4.

### 4.2. Line-width measurements

We measured the line width (using both the FWHM and line dispersion  $\sigma_{\text{H}\beta}$  parameters) of the broad H $\beta$  for both the mean and rms spectra. The narrow-line contributions in the rms spectra are fairly weak for all of the targets, thus the corresponding FWHM and  $\sigma_{\text{H}\beta}$  of the rms spectra can be obtained easily. We measured the H $\beta$  profiles after subtracting continuum; continuum windows were selected beyond any contribution from the emission lines and can differ between the mean and rms profiles and from the ones listed in Table 2, which were optimized for light curves. However, before measuring the H $\beta$  widths from the mean spectra, the narrow H $\beta$  and [O III] $\lambda$ 4959, 5007 lines still do need to be removed.

We first assumed that all of the three narrow lines (H $\beta$  and [O III] $\lambda$ 4959, 5007) have the same profile. Since the blue wing of [O III] $\lambda$ 5007 can be slightly blended with the red wing of [O III] $\lambda$ 4959 (see Figure 2), we started by removing the [O III] $\lambda$ 4959 by shifting and scaling the [O III] $\lambda$ 5007 line (after subtracting the local continuum background determined from the interpolation of two nearby windows). Then, the corrected [O III] $\lambda$ 5007 profile was extracted from the [O III] $\lambda$ 4959-subtracted spectrum, and was treated as the template of the narrow-line profile. We obtained the narrow component of the H $\beta$  line by fitting the spectrum in a very narrow and local window around 4861Å (not the entire H $\beta$  profile) with the narrow-line template, a Gaussian (a second Gaussian was added if necessary), and a linear background. The Gaussian(s) + linear background is used to account for the contribution from the broad H $\beta$  in the narrow window (the top part of the broad H $\beta$ ). Because the H $\beta$  profile in the

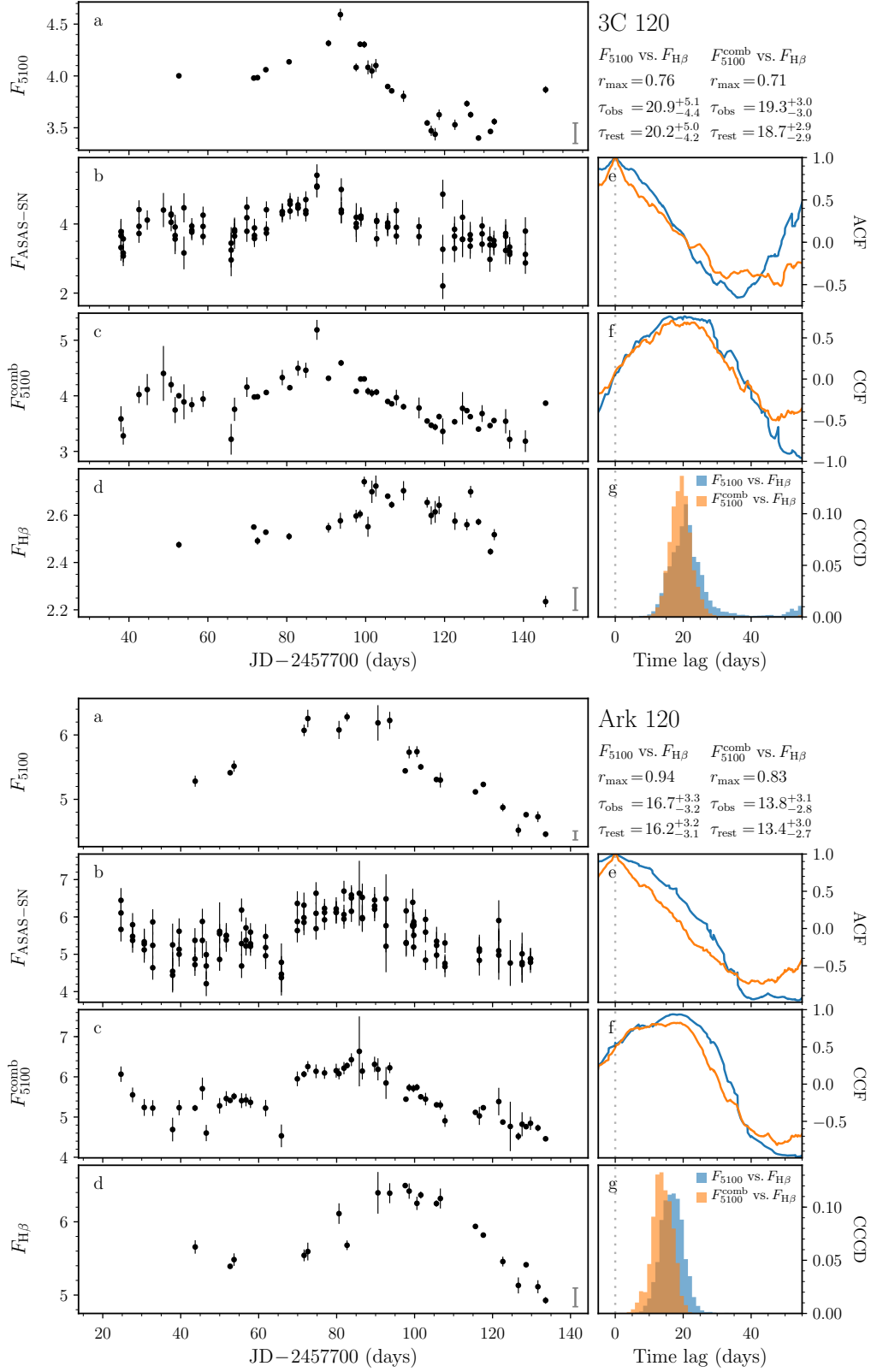


**Figure 3.** Light curves and cross-correlation functions. Panel a, b, c, and d are the continuum at  $5100\text{\AA}$ , photometry from ASAS-SN, combined continuum, and  $H\beta$  light curves. Panel e, f, and g are ACF, CCF, and CCCD. The name of the object and the corresponding lag measurements in both of the observed and rest frames are marked in the upper-right corner of the figure. The units of the continuum and emission-line light curves are  $10^{-15} \text{ erg s}^{-1} \text{ cm}^{-2} \text{ \AA}^{-1}$  and  $10^{-13} \text{ erg s}^{-1} \text{ cm}^{-2}$ , respectively. Systematic errors are added if needed and shown as the gray error bars in the lower-right corners in panels a – d (see more details in Section 3).

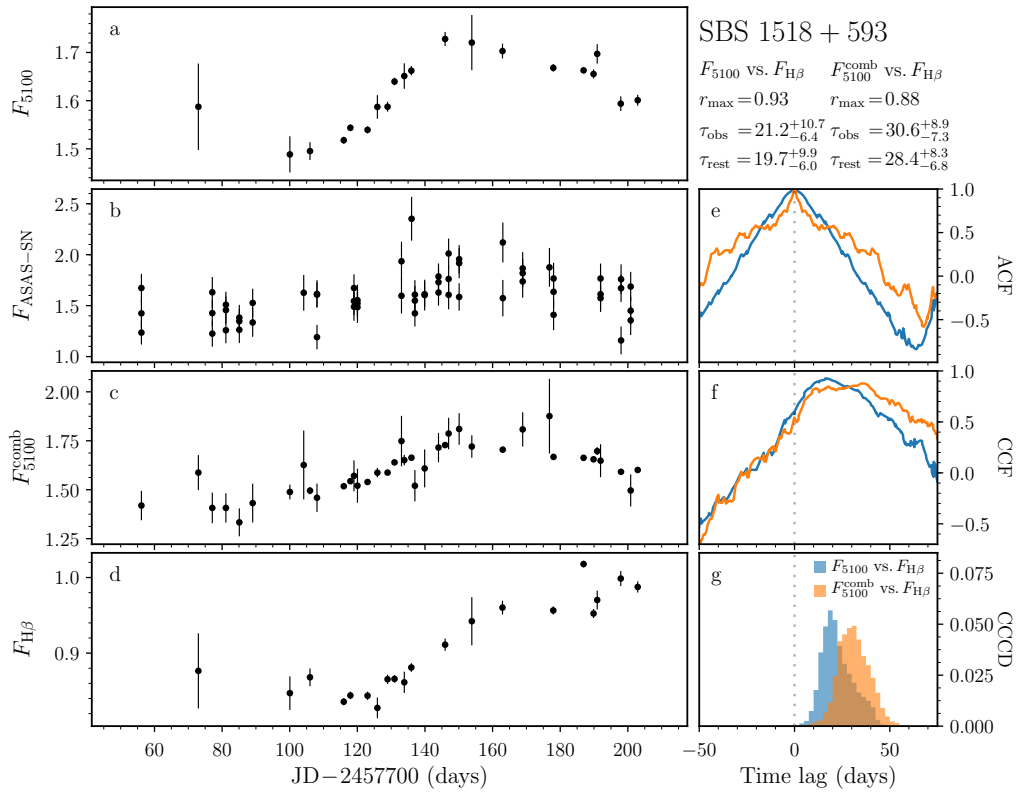
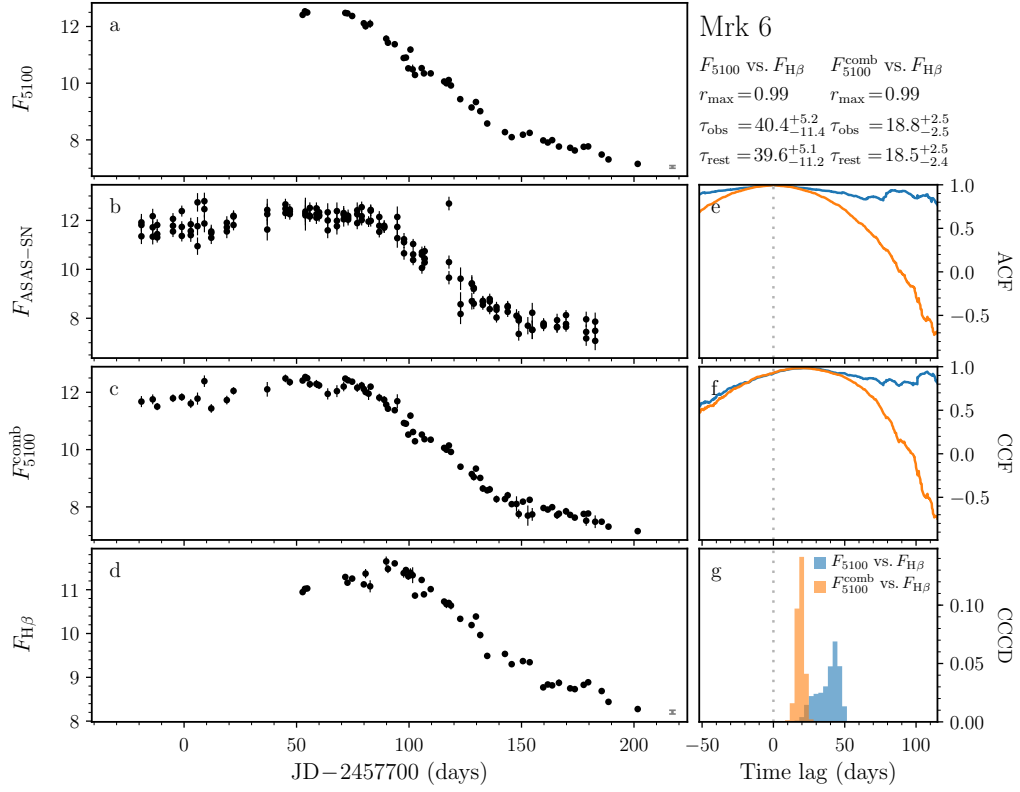


Figure 3. (Continued.)

present sample is very complex and asymmetric, we did not fit the entire profile but a narrower and local window (usually a window of  $4000 \sim 5000 \text{ km s}^{-1}$ ) around  $4861 \text{ \AA}$ . We tried to add more Gaussians or changed the Gaussian(s) to a high-order polynomial as the broad  $H\beta$  contribution in the fitting, but the fitting results and the following width measurements did not change significantly because the shape of the narrow template has been constrained by the corresponding  $[\text{O III}]\lambda 5007$  profile of each object. Table 5 provides the narrow  $[\text{O III}]\lambda 5007/H\beta$  and  $[\text{O III}]\lambda 5007/[\text{O III}]\lambda 4959$  flux ratios obtained by this procedure, and Figure 2 shows the narrow-line-subtracted  $H\beta$  profiles for the mean spectra. The  $[\text{O III}]\lambda 5007/H\beta$  and  $[\text{O III}]\lambda 5007/[\text{O III}]\lambda 4959$  ratios are close to the typical values (3 and 10, respectively, e.g., Kewley et al. 2006; Stern & Laor 2013) in AGNs, which means that the narrow-line subtraction procedure adopted here appears to work well. Then we measured the FWHM and  $\sigma_{H\beta}$  from the mean  $H\beta$  profiles after the narrow-line subtraction.

We estimated the broad  $H\beta$  velocity width uncertainties for both the mean spectra and the rms spectra by using the bootstrap method. A subset spectrum was created by resampling  $N$  points with replacement from the  $N$  data points in the mean/rms spectrum. For the rms spectrum, we measured the FWHM and  $\sigma_{H\beta}$  from the subset spectrum, and repeated the resampling and the measurement 500 times to generate the FWHM and  $\sigma_{H\beta}$  distributions. The resulting median values and the standard deviations of the distributions were regarded as the measurements and the uncertainties. For the mean spectrum, we subtracted the narrow lines from the subset spectrum by using the procedure described above before the measuring the widths. The uncertainties of the narrow-line flux ratios in Table 5 were also obtained at the same time.

To estimate the width of the line spread function (instrumental broadening) in our observations, we measured the widths of the  $[\text{O III}]$  lines in the mean spectra and compared them with the intrinsic narrow-line widths in Whittle (1992) or the higher resolution spectra of the Sloan Digital Sky Survey (SDSS). The FWHM of the line spread function obtained for different object ranges from  $\sim 850 \text{ km s}^{-1}$  to  $\sim 1000 \text{ km s}^{-1}$ . For simplicity, we adopted the mean value of  $925 \text{ km/s}$  (FWHM) as the line spread function for all of the objects in our campaign. After correcting the contribution of the line spread function, the line widths (FWHM and  $\sigma_{H\beta}$ ) of the  $H\beta$  in the mean and rms spectra are listed in Table 6.

#### 4.3. Black hole masses and accretion rates

Combining the time lag with the line width measured from the FWHM or line dispersion, the black hole mass can be obtained by the Equation 1. For AGNs with extreme BLR kinematics, e.g., super-fast or ultra-strong inflow or outflow, or extreme inclination angles, the virial factor  $f_{\text{BLR}}$  may possibly differ significantly from typical values (e.g., Pancoast et al. 2014).

The mean  $f_{\text{BLR}}$  of a sample can be calibrated by comparing the RM objects, which have bulge stellar velocity dispersion measurements ( $\sigma_*$ ), with the  $M_\bullet - \sigma_*$  relation of the inactive galaxies (e.g., Onken et al. 2004; Woo et al. 2010,

2015; Park et al. 2012; Grier et al. 2013a; Ho & Kim 2014, see a brief review in Du et al. 2017). However, each individual object may have a very different virial factor (e.g., Horne 1994; Horne et al. 2004; Bentz et al. 2010; Grier et al. 2013b; Pancoast et al. 2014), especially for those AGNs with asymmetric  $H\beta$  profiles which may host BLRs with complex geometry or kinematics. We adopt  $f_{\text{BLR}} = 1.12, 4.47$  in Woo et al. (2015) corresponding to the FWHM and  $\sigma_{H\beta}$  in the rms spectra, respectively, and also provide simple virial products (assuming  $f_{\text{BLR}} = 1$ ) for the FWHM measurements in the mean spectra for the present sample in Table 6, but acknowledge the potentially large uncertainty on  $f_{\text{BLR}}$ . The uncertainties of the black hole masses listed in Table 6 only account for the error bars of the lag and width measurements.

We provide general estimates of their dimensionless accretion rates, defined as  $\dot{\mathcal{M}} = \dot{M}_\bullet / L_{\text{Edd}} c^{-2}$ , where  $\dot{M}_\bullet$  is the mass accretion rate and  $L_{\text{Edd}}$  is the Eddington luminosity (Du et al. 2015, 2016b). The  $\dot{\mathcal{M}}$  can be estimated by using the formula (see more details in Du et al. 2015, 2016b)

$$\dot{\mathcal{M}} = 20.1 \left( \frac{\ell_{44}}{\cos i} \right)^{3/2} m_7^{-2}, \quad (6)$$

where  $\ell_{44} = L_{5100}/10^{44} \text{ erg s}^{-1}$  is the monochromatic luminosity at  $5100 \text{ \AA}$ ,  $m_7 = M_\bullet/10^7 M_\odot$ , and  $i$  is the inclination angle of disk to the line of sight. We adopted  $\cos i = 0.75$  (see some discussions in Du et al. 2016b), which is an average estimate for type I AGNs (e.g., Pancoast et al. 2014). For the most precise results, it is necessary to subtract the host contribution from  $L_{5100}$  before calculating the accretion rates, but this is beyond the present scope of this paper, so our estimates are upper limits. We found  $\dot{\mathcal{M}} \lesssim 1 \sim 2$  for 3C 120 and SBS 1518+593, and  $\lesssim 0.2$  for Ark 120 and Mrk 6. Therefore, all of the 4 objects are sub-Eddington accretors. More detailed determinations of luminosity will be done in a future paper allowing more precise estimates.

#### 4.4. Velocity-resolved time lags

In order to investigate the geometry and kinematics of their BLRs, we measure the velocity-resolved time lags of the  $H\beta$  emission lines of our target AGNs. Several typical transfer function models and their corresponding velocity-resolved time lags are given by, e.g., Bentz et al. (2009), and more complicated examples of the transfer function are provided by, e.g., Welsh & Horne (1991) and Horne et al. (2004). In general, longer lags in the high-velocity blue/red part of the emission line are regarded as the signatures of inflow/outflow, while a symmetric velocity-resolved structure around zero velocity, with smaller time lags for higher velocities, is diagnostic of Keplerian disk or at least virialized motion over a spatially extended BLR in general. We divided the  $H\beta$  lines into several velocity bins, each of which having the same integrated fluxes in their individual continuum-subtracted rms spectra based on interpolation between the windows shown in Figure 2. Then, we measured the light curve in each bin and performed an ICCF analysis (using the method in Section 4.1) with the  $5100 \text{ \AA}$  continuum light curve

**Table 6.**  $H\beta$  Width Measurements and Black Hole Masses

Object	mean spectra		rms spectra		$M_{\text{VP}}$ (mean spectra)	$M_{\bullet}$ (rms spectra)	
	$V_{\text{FWHM}}$	$\sigma_{\text{line}}$	$V_{\text{FWHM}}$	$\sigma_{\text{line}}$	$R_{H\beta} V_{\text{FWHM}}^2/G$	$1.12 \times R_{H\beta} V_{\text{FWHM}}^2/G$	$4.47 \times R_{H\beta} \sigma_{\text{line}}^2/G$
	( $\text{km s}^{-1}$ )	( $10^7 M_{\odot}$ )	( $10^7 M_{\odot}$ )	( $10^7 M_{\odot}$ )			
3C 120	$3711 \pm 34$	$3174 \pm 32$	$2343 \pm 26$	$1360 \pm 42$	$5.43^{+1.35}_{-1.13}$	$2.43^{+0.60}_{-0.51}$	$3.26^{+0.83}_{-0.71}$
Ark 120	$6487 \pm 16$	$3929 \pm 14$	$5247 \pm 25$	$2184 \pm 31$	$13.31^{+2.63}_{-2.55}$	$9.75^{+1.93}_{-1.87}$	$6.75^{+1.35}_{-1.30}$
Mrk 6	$5457 \pm 16$	$3647 \pm 29$	$5274 \pm 22$	$3300 \pm 30$	$10.76^{+1.46}_{-1.40}$	$11.25^{+1.52}_{-1.46}$	$17.59^{+2.40}_{-2.30}$
SBS 1518+593	$3374 \pm 17$	$2429 \pm 37$	$2499 \pm 22$	$1038 \pm 20$	$4.38^{+2.20}_{-1.33}$	$2.69^{+1.35}_{-0.82}$	$1.85^{+0.93}_{-0.57}$

NOTE—The line spread function caused by the instrument and seeing has been corrected from the line-width measurements.  $M_{\text{VP}}$  is the virial product measured from the mean spectrum (see more details in Section 4.3). The black hole masses ( $M_{\bullet}$ ) are calculated from the rms spectra using the  $f_{\text{BLR}}$  factors in Woo et al. (2015).

(the combined continuum light curve in the case of Mrk 6). Figure 4 shows the resulting time lags as a function of the velocity and the corresponding rms spectrum for each object.

The velocity bins with equal rms flux have the same level of variation but may have different amounts of physical flux. As a further test, we divided the  $H\beta$  lines into the velocity bins, each of which having the same  $H\beta$  fluxes in the narrow-line-subtracted mean spectra, and measured the velocity-resolved lags in Appendix B. In general, the results are almost the same as the rms-based velocity-resolved lags, which means the velocity-resolved analysis here is robust. In the following Section 5, the discussion of their BLRs is based on the results in Figure 4.

## 5. DISCUSSION

Our data have produced integrated  $H\beta$  time lags as well as high-quality velocity-resolved time lags for our four featured AGNs. We discuss each object individually below and compare our results to past work as appropriate.

### 5.1. Individual Objects

#### 5.1.1. 3C 120

As a nearby broad-line radio galaxy, its mean  $H\beta$  profile is asymmetric toward the red, however the rms  $H\beta$  profile is strongly blueshifted (see Figures 2 and 4). Its  $H\beta$  time lag respect to the varying continuum was first detected successfully by Peterson et al. (1998), albeit with large uncertainty, and the measured lag was  $43.8^{+27.7}_{-20.3}$  days in the rest frame. After  $\sim 11$  years, it was monitored again in 2008 – 2009, and the observed rest-frame  $H\beta$  time lag was  $27.9^{+7.1}_{-5.9}$  days (Kollatschny et al. 2014). 3C 120 was observed the third time with higher temporal sampling in 2010 – 2011, and a similar  $H\beta$  delay of  $25.9^{+2.3}_{-2.3}$  days in the rest frame was obtained from the light curves by using CCF analysis method (Grier et al. 2012). From the velocity-resolved time lag measurement and the transfer function reconstructed by the maximum entropy method (Grier et al. 2013b), its BLR was likely an inclined disk or a spherical shell, but there was also some evidence of inflow given that the strength of its line response was asymmetric (Grier et al. 2013b).

Our campaign was carried out  $\sim 7$  years later than the observation in Grier et al. (2012), and captured a very strong

peak around Julian date  $\sim 90$  days (from the zero point of 2457700 in Figure 3) in the continuum and a clear response around  $\sim 110$  days in the  $H\beta$  light curve. The detected  $H\beta$  lag is  $20.2^{+5.0}_{-4.2}$  days in the rest frame, which is slightly shorter than the value in Grier et al. (2012), but the difference is not significant considering the uncertainties. In addition, the rms spectrum in our campaign is different from that in Grier et al. (2012). Our rms spectrum is significantly blueshifted (see Figure 4), while the rms spectrum in Grier et al. (2012) has a strong red asymmetry. This implies that the varying part of the BLR in 3C 120 has significantly changed after  $\sim 7$  years.

Furthermore, the velocity-resolved lag measurement shows a complicated structure, which is different from the symmetric velocity-resolved results of a inclined disk or a spherical shell determined by Grier et al. (2013b). From  $1500 \text{ km s}^{-1}$  to  $-1500 \text{ km s}^{-1}$ , the lag gradually decreases, which is the signature of outflow. However, the tendency changes around  $\sim 1500 \text{ km s}^{-1}$ , and the lags become longer at the blue end. This complicated structure suggests that its BLR is in a complex state. Of course, it should be noted that only the two bins (with a little larger uncertainties) at the highest blue velocities are in charge of the upturn at the blue side. More observations with better spectral resolution and higher S/N ratios are needed in the future to verify this complex state and to investigate the detailed BLR kinematics.

#### 5.1.2. Ark 120

Given its asymmetric/double-peak  $H\beta$  profile and the long-term periodic-like variation in past decades, Ark 120 is a possible candidate for a supermassive black hole binary system (Li et al. 2017). Its  $H\beta$  time lags during 1990 September – 1991 March and 1995 September – 1996 April, measured by Peterson et al. (1998, 2004), were  $47.1^{+8.3}_{-12.4}$  days and  $37.1^{+4.8}_{-5.4}$  days in the rest frame, respectively. Doroshenko et al. (2008) monitored this object from 1992 to 2005, and obtained an  $H\beta$  lag of  $70 \pm 7$  days in the rest frame, by combining their data with other additional data from 1988 to 1996 (Peterson et al. 1998).

During our campaign, the mean spectrum of Ark 120 was not significantly double-peaked, but the rms spectrum shows clearly two peaks. One is located at roughly  $4861 \text{ \AA}$  in the rest frame, and the other is strongly redshifted by  $\sim 2500$

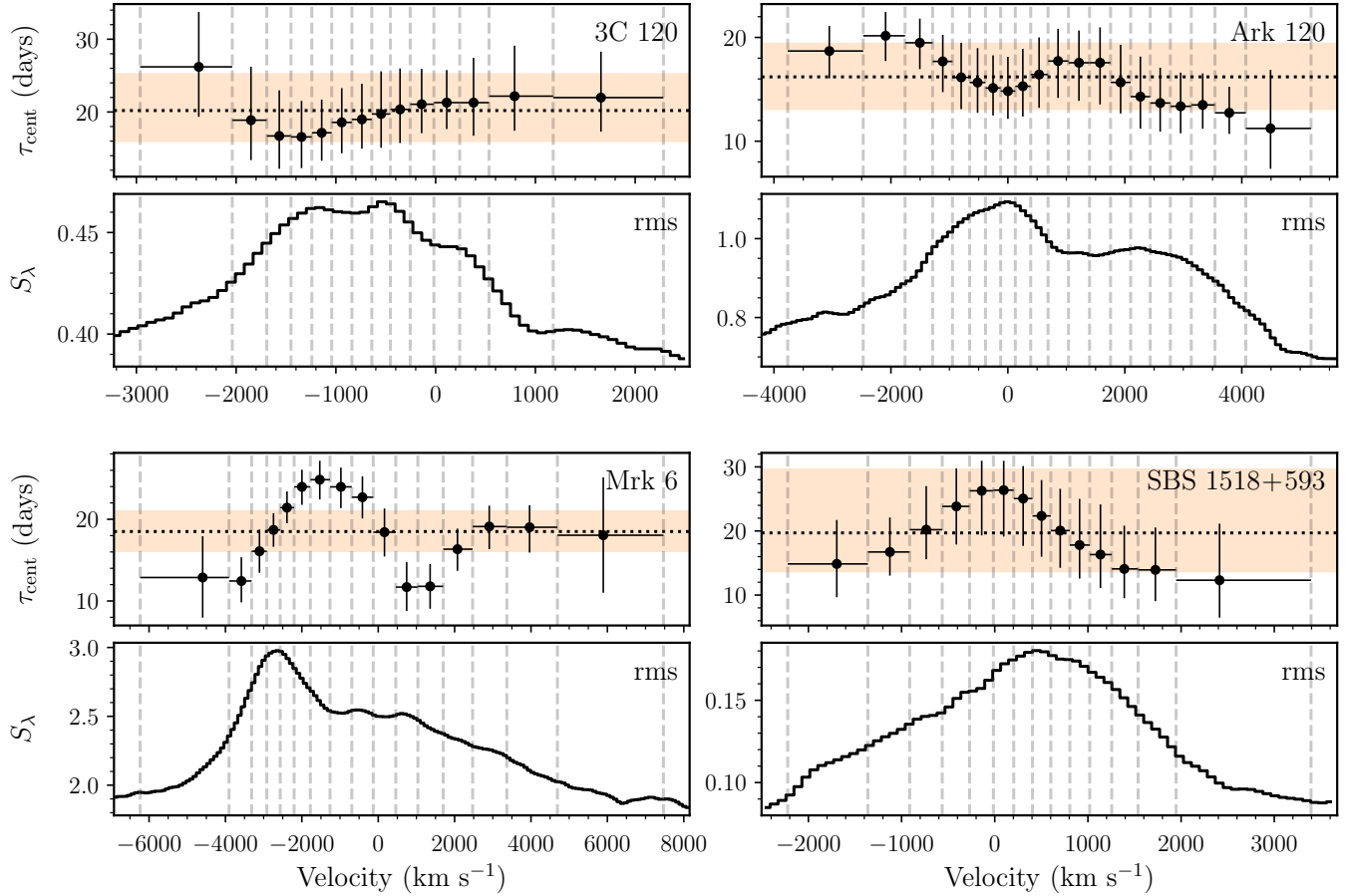


**Figure 4.** Rest-frame velocity-resolved time lags and the corresponding rms spectra. The upper panel in each plot shows the centroid lags at different velocities, and the lower panel is the rms spectrum in unit of  $10^{-15} \text{ erg s}^{-1} \text{ cm}^{-2} \text{ \AA}^{-1}$ . The name of the object is marked in the upper-right corner of each plot. The vertical dashed lines are the edges of velocity bins. The horizontal dotted lines and the orange color are the average time lags and the uncertainties in Table 4.

$\text{km s}^{-1}$ . The rms spectrum is different from the one in Peterson et al. (1998). The rms spectrum in Peterson et al. (1998) has three peaks (an additional blueshifted peak), and the redshifted peak is relatively stronger. One simple and reasonable guess is that both of the blueshifted and redshifted peaks became relatively weaker with respect to the peak with zero velocity by the epoch of our campaign, which implies a possible correlation between the origins of these two peaks.

Our velocity-resolved lag measurement of Ark 120 is also complicated. In general, the time lag decreases from the blue ( $-3000 \text{ km s}^{-1}$ ) to the red ( $4000 \text{ km s}^{-1}$ ) velocity, which is the signature of an inflowing BLR. However, there is a local peak around  $1000 \sim 2000 \text{ km s}^{-1}$ , which corresponds to the dip between the two peaks in the rms spectrum. To further investigate the geometry and kinematics of the BLR in Ark 120, reconstructing its velocity-delay map is needed. We will reconstruct the velocity-delay map of the objects in the present sample using the maximum entropy method (e.g., Horne 1994) in a separate paper in the near future.

### 5.1.3. Mrk 6

It has been known for more than 40 years that the  $\text{H}\beta$  profile of Mrk 6 is extremely asymmetric and has a blueshifted peak with the velocity of  $\sim -3000 \text{ km s}^{-1}$  (Khachikian & Weedman 1971). With its strange radio morphology (jet flips and jet precession as reported by, e.g., Kukulka et al. 1996; Kharb et al. 2014), Mrk 6 is suggested to be a potential supermassive binary black hole system (Kharb et al. 2014).

Mrk 6 has been spectroscopically monitored by different groups in the past decades (Sergeev et al. 1999; Doroshenko & Sergeev 2003; Doroshenko et al. 2012; Grier et al. 2012). With the long temporal span of the campaign (1992 – 2008), Doroshenko et al. (2012) found the time lag of its  $\text{H}\beta$  line to be  $21.1 \pm 1.9$  days in the rest frame. Grier et al. (2012) observed this object again in 2010 with a higher sampling rate, and obtained a different  $\text{H}\beta$  lag of  $10.1 \pm 1.1$  days. In our observation, the new  $\text{H}\beta$  time lag is  $18.5^{+2.5}_{-2.4}$  days in the rest frame, which is more similar to the result of Doroshenko et al. (2012). Moreover, the line width ( $\text{FWHM} = 5274 \text{ km s}^{-1}$ ) in our rms spectrum is similar to the value ( $5445 \text{ km s}^{-1}$ ) in Doroshenko et al. (2012), and much smaller than the number ( $9744 \text{ km s}^{-1}$ ) in Grier et al. (2012). These changes might

be simply due to the BLR “breathing” effect (e.g., Peterson et al. 2002; Korista & Goad 2004; Cackett & Horne 2006).

Considering the very complex  $H\beta$  profile of this object, it is interesting to compare the rms spectrum and the velocity-resolved time lags in our campaign with those reported by Doroshenko et al. (2012) and Grier et al. (2012). Doroshenko et al. (2012) found that the rms spectrum had two prominent peaks (one is blueshifted and the other has roughly zero velocity) during 1993 – 1999. The two peaks in the rms spectrum almost disappeared in 2000 – 2002, and rose again in 2005 – 2008 (Doroshenko et al. 2012). A third small peak with redshifted velocity ( $\sim 1500 \text{ km s}^{-1}$ ) appeared in 2005 – 2008, which makes the things even more complex. Grier et al. (2012) found that the blueshifted peak became strong again in 2010, and the redshifted peak was also still significant. It should be noted that the blueshifted peak always stayed at  $\sim -3000 \text{ km s}^{-1}$ , and did not show large velocity changes, however, its relative intensity has changed significantly with time (Doroshenko et al. 2012; Grier et al. 2012).

The velocity-resolved time lag measurements of Mrk 6 also shows very complex structures (Doroshenko et al. 2012; Grier et al. 2013b). Doroshenko et al. (2012) found that the velocity-resolved lags are generally shorter in the wings and longer in the line core, but the longest lag is blueshifted by  $\sim -2000 \text{ km s}^{-1}$ . They interpreted this complex velocity-resolved lag measurement as a combination of virial motion plus inflowing gas. The velocity-resolved lags in Grier et al. (2013b) are similar to the results for 1993 – 1995 in Doroshenko et al. (2012), but the lags increase gradually from  $2000 \text{ km s}^{-1}$  to  $7500 \text{ km s}^{-1}$ . Our velocity-resolved lags are more similar to the results of Grier et al. (2013b), that the longest lag is located at  $-2000 \text{ km s}^{-1}$  and the lags increase from  $1500 \text{ km s}^{-1}$  to  $7000 \text{ km s}^{-1}$ . It is not easy to simply explain this complicated velocity-resolved lag structure using a combination of virial motion and inflowing gas suggested by Doroshenko et al. (2012). Thus, the velocity-delay map and detailed modeling of a more complex BLR geometry and kinematics are needed to further explore the nature of this object. It should be noted that the bin with the highest velocity on the red side has relatively larger uncertainty, which may be caused by the slight influence from the  $[\text{O III}]\lambda 4959$  line. We will conduct the observation in the future to check this issue.

Mrk 6 has the longest monitoring period, the highest sampling rate, and the best S/N ratios among the 4 objects in the present paper. Although the continuum of Mrk 6 changes very slowly (rise slowly in the first half and then shows a gently falling trend, see panel c in Figure 3), which makes its ACF and CCF exceptionally broad (see also Figure 3), the uncertainties of its time lag measurement produced by the FR/RSS method (Peterson et al. 1998, 2004) are still acceptable. But it should be pointed out that the very slow variation in the continuum and the corresponding broad ACF/CCF may potentially limit the smallest observable lag, either probing different parts of the BLR or skewing the gas distribution to respond to larger radii (Goad & Korista 2015). The future observation will investigate this possibility.

#### 5.1.4. SBS 1518+593

The time lag of SBS 1518+593 is mainly determined by the dip around 105 days in the continuum light curve and the response around 125 days in the  $H\beta$  light curve. The peak at  $\sim 150$  days in the continuum and its potential response at  $\sim 180$  in the emission-line light curve also provide constraint to the lag measurement, but only play a minor role because the peak in the  $H\beta$  light curve is already near to the end of the campaign.

The  $H\beta$  emission line in the mean spectrum of SBS 1518+593 is asymmetric toward the red wing, whereas the peak of the  $H\beta$  in the rms spectrum is mildly redshifted (see Figure 2). However, its velocity-resolved lag measurement is not significantly asymmetric. The longer lags in the line core and the shorter lags in the line wings imply that the geometry and kinematics of its BLR tend to be virialized motion or a Keplerian disk.

#### 5.2. Ongoing project

Our primary objectives are: (1) revealing the complex BLR physics behind AGNs with asymmetric  $H\beta$ , (2) understanding the influence of differing BLR geometry or kinematics for the black hole mass measurement, and (3) looking for SMBH binary systems.

In particular, with the data quality and calibration precision improving in recent years, the velocity-resolved RM, including the velocity-resolved time lag measurements (e.g., Bentz et al. 2008, 2009, 2010; Denney et al. 2009, 2010; Grier et al. 2013b; Du et al. 2016a) and the analysis of the velocity-delay maps reconstructed through the maximum entropy method (e.g., Horne 1994; Horne et al. 2004; Bentz et al. 2010; Grier et al. 2013b), regularized linear inversion (Skjelboe et al. 2015), or Bayesian-based dynamical modeling by Markov Chain Monte Carlo (MCMC) method (e.g., Pancoast et al. 2011, 2012, 2014; Grier et al. 2017a), was successfully applied to more than 20 AGNs, and preliminarily revealed the geometry and kinematics of their BLRs. We plan to significantly add to this total and help make a breakthrough in our understanding.

### 6. SUMMARY

In this paper, we describe the MAHA project and report some results from the first campaign. We successfully obtained the  $H\beta$  time lags of 4 objects observed from December 2016 to May 2017, and preliminarily investigated their BLR kinematics through measuring the velocity-resolved lags. The velocity-resolved results of 3C 120, Ark 120, and Mrk 6 showed very complex structures, which were different from the simple signatures of outflow, inflow, or virialized motion. The velocity-resolved lag measurements of SBS 1518+593 showed generally shorter lags in the line wings and longer ones at the line centers, which implied that their BLR is virialized motion or a Keplerian disk. The complexities of the velocity-resolved time lags in the AGNs with asymmetric  $H\beta$  line profiles clearly demonstrate the very complex geometry and kinematics of their BLRs, and

**Table 7.** MAHA Targets

Object	$\alpha_{2000}$	$\delta_{2000}$	Redshift	Mag	Asymmetry
III Zw 2	00 10 30.8	+10 58 13	0.0898	15.4	-0.141
Mrk 1148	00 51 54.7	+17 25 59	0.0640	15.5V	-0.033
SDSS J015530.01-085704.0	01 55 30.0	-08 57 04	0.1644	16.9g	0.060
NGC 985	02 34 37.8	-08 47 15	0.0431	13.8	-0.050
SDSS J023922.87-000119.5	02 39 02.9	-00 01 29	0.2616	15.9R	-0.213
3C 120	04 33 11.1	+05 21 16	0.0330	14.1r	-0.187
Ark 120	05 16 11.4	-00 08 59	0.0327	15.3b	-0.185
Mrk 6	06 52 12.2	+74 25 37	0.0188	15.0	-0.352
NGC 2617	08 35 38.8	-04 05 18	0.0142	14	-0.169
SDSS J093653.84+533126.8	09 36 53.8	+53 31 27	0.2278	17.1g	-0.113
SDSS J094603.94+013923.6	09 46 03.9	+01 39 24	0.2199	17.8g	0.383
PG 0947+396	09 50 48.4	+39 26 51	0.2059	16.3g	-0.117
SDSS J095539.81+453217.0	09 55 39.8	+45 32 17	0.2594	16.9g	-0.052
Mrk 715	10 04 47.6	+14 46 46	0.0846	16.6g	-0.149
PG 1004+130	10 07 26.1	+12 48 56	0.2406	15.4g	-0.223
PG 1048+342	10 51 43.9	+33 59 27	0.1670	16.8g	-0.246
PG 1100+772	11 04 13.7	+76 58 58	0.3115	15.5B	-0.206
PG 1151+117	11 53 49.3	+11 28 30	0.1761	16.4g	-0.224
PG 1202+281	12 04 42.1	+27 54 12	0.1653	17.2g	-0.351
PG 1302-102	13 05 33.0	-10 33 19	0.2784	14.9V	-0.218
VIII Zw 233	13 05 34.5	+18 19 33	0.1180	16.8g	-0.001
PG 1309+355	13 12 17.8	+35 15 21	0.1829	15.8g	-0.424
WISE J134617.54+622045.3	13 46 17.5	+62 20 45	0.1167	16.9g	-0.303
PG 1351+640	13 53 15.8	+63 45 46	0.0882	14.5V	-0.232
SBS 1518+593	15 19 21.6	+59 08 24	0.0781	15.8g	-0.077
SDSS J152139.66+033729.2	15 21 39.7	+03 37 29	0.1265	17.1g	-0.247
MRK 876	16 13 57.2	+65 43 10	0.1290	14.3V	-0.206
SDSS J171448.50+332738.2	17 14 48.5	+33 27 38	0.1812	16.9g	-0.213
3C 390.3	18 42 09.0	+79 46 17	0.0561	14.37	-0.062
2MASX J21140128+8204483	21 14 01.2	+82 04 48	0.0840	15.7	0.019

NOTE— Positions, redshifts, and magnitudes are from the NASA/IPAC Extragalactic Database (NED), except for the magnitude of III Zw 2, for which NED has no entry. We have provided our own estimate of 15.4. We have calculated asymmetries using measurements of new single-epoch WIRO spectra shown in Figure 5 and the formula of De Robertis (1985).

provide good opportunities to understand the physics of the BLRs in AGNs in more details in the future.

We thank the anonymous referee for constructive comments. We acknowledge the support by National Key R&D Program of China (grants 2016YFA0400701 and 2016YFA0400702), by NSFC through grants NSFC-11503026, -11233003, -11573026, -11773029, by the Strategic Priority Research Program of the Chinese Academy of Sciences

Grant No. XDB23000000, and by Grant No. QYZDJ-SSW-SLH007 from the Key Research Program of Frontier Sciences, CAS. This research has made use of the NASA/IPAC Extragalactic Database (NED), which is operated by the Jet Propulsion Laboratory, California Institute of Technology, under contract with the National Aeronautics and Space Administration. We thank WIRO engineer James Weger for his invaluable assistance.

## APPENDIX

### A. MAHA TARGETS

We present our initial suite of MAHA targets in order of Right Ascension in Table 7, and plot recent WIRO spectra in Figure 5. The WIRO spectra displayed in Figure 5 have had their narrow lines subtracted as described in the main text.

Below are notes on individual objects in alphanumeric order by name.

*2MASX J21140128+8204483*. Also known as S5 2116+81, the  $H\beta$  profile displays a significant blue asymmetry.

*3C 120*. One of the objects featured in this paper and possessing an  $H\beta$  line with a red asymmetric tail. *3C 120* has been previously reverberation mapped several times, with recent results published by Grier et al. (2012).

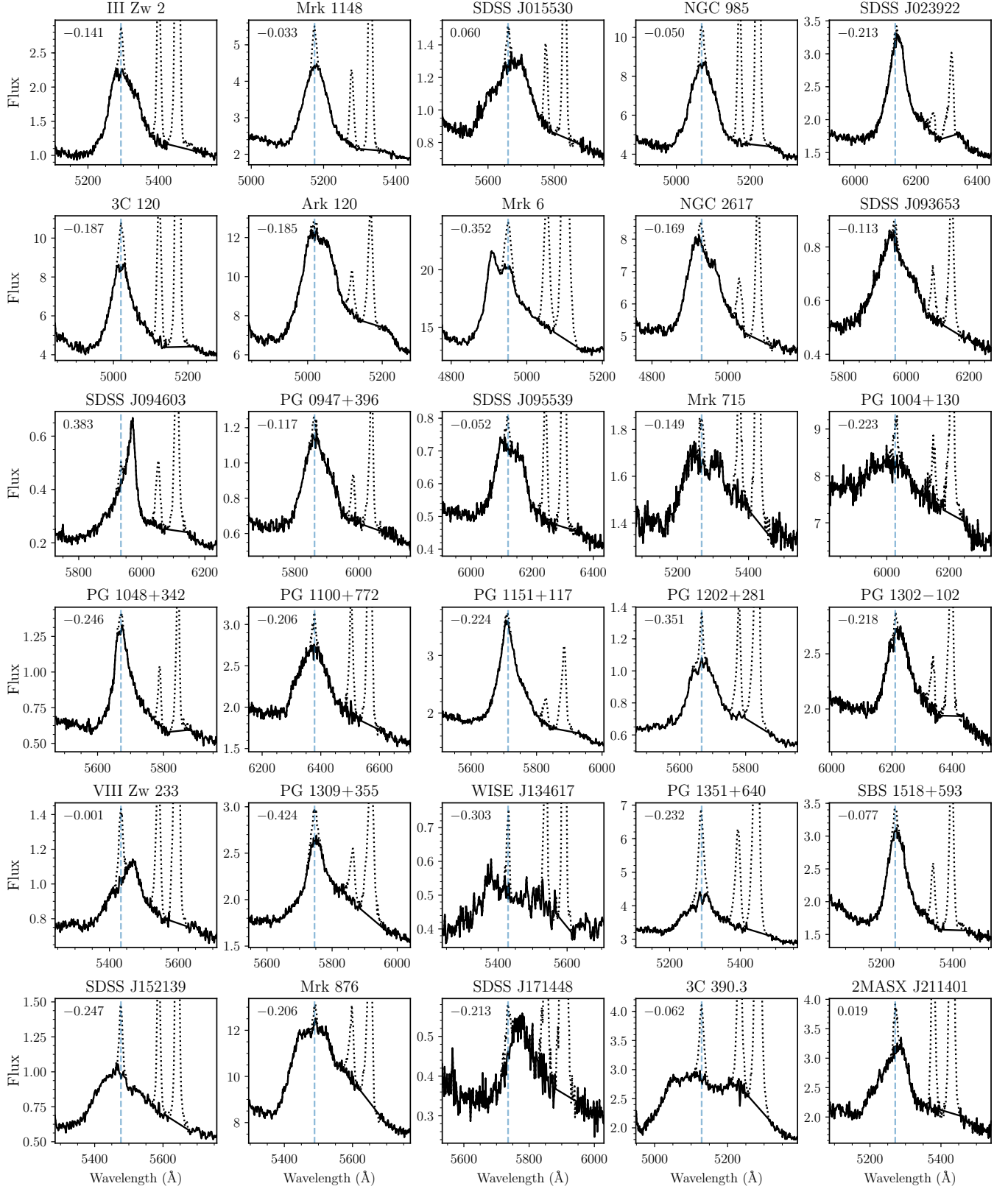


**Figure 5.** WIRO spectra of the targets listed in Table 7. The solid lines are the narrow-line-subtracted H $\beta$  profiles, and the dotted lines are the narrow H $\beta$ , [O III] $\lambda$ 4959, 5007 lines. The asymmetry  $A$  of each object is marked in the upper-left corner. The unit of flux is  $10^{-15}$  erg s $^{-1}$  cm $^{-2}$  Å $^{-1}$ .

*3C 390.3*. Others have previously reverberation mapped this object, which displays double-peaked emission lines (e.g., [Shapovalova et al. 2010](#); [Dietrich et al. 2012](#); [Sergeev et al. 2017](#)). *3C 390.3* once displayed quasi-periodic emission-line profile changes suggestive of a binary ([Gaskell 1996](#)), but later deviated from the predicted pattern ([Eracleous et al. 1997](#)).

*III Zw 2*. This object has an  $H\beta$  profile with an extreme red asymmetry.

*Ark 120*. One of the objects featured in this paper, displaying a broad and complex double-peaked  $H\beta$  profile. Previous RM results exist in the literature (e.g., [Peterson et al. 1998](#); [Doroshenko et al. 2008](#)).

*Mrk 6*. One of the objects featured in this paper and possessing a highly blueshifted peak and a red tail, probably also double-peaked at the present epoch. There has been high-quality RM at previous epochs ([Doroshenko et al. 2012](#); [Grier et al. 2012](#)).

*Mrk 715*. Also known as SDSS J100447.61+144645.6, this object has a double-peaked  $H\beta$  line profile and a long tail to the red.

*Mrk 876*. The current  $H\beta$  profile is suggestive of a double-peaked profile with red asymmetry. In the past ([De Robertis 1985](#)), the blueshifted peak was significantly stronger, reminiscent of *Mrk 6*.

*Mrk 1148*. This object has an  $H\beta$  profile with a mild red asymmetry.

*NGC 985*. This object has an  $H\beta$  profile with a red asymmetry.

*NGC 2617*. Recently [Fausnaugh et al. \(2017\)](#) published RM of this object. Interestingly, their work covering the 2014 epoch shows the  $H\beta$  profile has a significant bump on the *blue* side of the profile, while WIRO spectra in 2017 and 2018 show a bump on the *red* side of the profile.

*PG 0947+396*. The  $H\beta$  profile shows a red asymmetry.

*PG 1004+130*. This object is somewhat luminous ( $> 10^{45}$  ergs  $s^{-1}$ ) and a likely radio-loud broad absorption line quasar ([Wills et al. 1999](#)). The  $H\beta$  line has a red asymmetry.

*PG 1048+342*. This PG quasar has a red asymmetric  $H\beta$  profile.

*PG 1100+772*. This luminous PG quasar has a  $H\beta$  profile with a blue bump but a red tail.

*PG 1151+117*. The  $H\beta$  profile shows a red asymmetry.

*PG 1202+281*. Also known as GQ COM, this object has an  $H\beta$  profile with a red asymmetry.

*PG 1302-102*. This luminous radio-loud PG quasar has a red asymmetric  $H\beta$  profile. More notably, [Graham et al. \(2015\)](#) find a  $\sim 5$  year periodicity suggesting a binary nature, although [Liu et al. \(2018\)](#) suggest that the periodicity may have vanished. Time will tell.

*PG 1309+355*. This PG quasar has a red asymmetric  $H\beta$  profile, and appears particular well fit by two Gaussians suggesting two components.

*PG 1351+640*. This object has an  $H\beta$  profile with a bump on the blue side but also a long red wing. The bump seems to have weakened compared to the spectrum shown by [Boroson & Green \(1992\)](#) observed over 25 years previously.

*SBS 1518+593*. One of the objects featured in this paper, featuring a mild red asymmetry at the present epoch.

*SDSS J015530.01-085704.0*. The  $H\beta$  line has a significantly redshifted peak along with the customary associated blue asymmetry ([Eracleous et al. 2012](#)).

*SDSS J023922.87-000119.5*. The  $H\beta$  profile shows a red asymmetry.

*SDSS J093653.84+533126.8*. In SDSS spectra, this object has an  $H\beta$  profile very similar to that of SDSS J094603.94+013823.6, showing a redshifted peak and blue asymmetry. Since then, a redshifted component has weakened dramatically leaving an emission line that is much more symmetric ([Runnoe et al. 2017](#)). All that is left now of that strong component is a weak, redshifted bump.

*SDSS J094603.94+013823.6*. The  $H\beta$  line has a significantly redshifted peak along with the customary associated blue asymmetry ([Eracleous et al. 2012](#)). The shifting profile is still consistent with expectations for a CB-SMBH ([Runnoe et al. 2017](#)).

*SDSS J095539.81+453217.0*. The  $H\beta$  line has a flat top with a blueshifted peak and a red asymmetry.

*SDSS J152139.66+033729.2*. This object possesses an  $H\beta$  line with a red asymmetry.

*SDSS J171448.50+332738.2*. This object possesses an unusual  $H\beta$  line with a redshifted top and red asymmetric wing.

*VIII Zw 233*. The  $H\beta$  line has a significantly redshifted peak.

*WISE J134617.54+622045.3*. The  $H\beta$  line has a significantly blueshifted peak along with the customary red asymmetry ([Eracleous et al. 2012](#)). The profile is reminiscent of *Mrk 6*.

## B. VELOCITY-RESOLVED TIME LAGS BASED ON MEAN SPECTRA

The velocity-resolved lags in Section 4.4 are measured based on the velocity bins with equal flux in the rms spectrum, where the emission line in each bin have the same level of variation but not the physical flux. As a further test, we divided the  $H\beta$  lines into the velocity bins, each of which having the same  $H\beta$  fluxes in the narrow-line-subtracted mean spectra, and measured the velocity-resolved lags again. Figure 6 demonstrates the velocity-resolved lag measurements based on the mean spectra. Comparing with the rms-based results, the bins in high velocities become relatively narrower and the bins in low velocities become wider, because the  $H\beta$  profiles in the mean spectra are broader than those in the rms spectra for these objects (see Table 6). For *Mrk 6*, the red wing is located beneath the  $[O III]\lambda 4959$  (see Figure 6). We reduced the number of bins (compared with the rms-based result of *Mrk 6*) to make the bins wider that the highest velocity bin can exactly cover the  $[O III]\lambda 4959$  in order

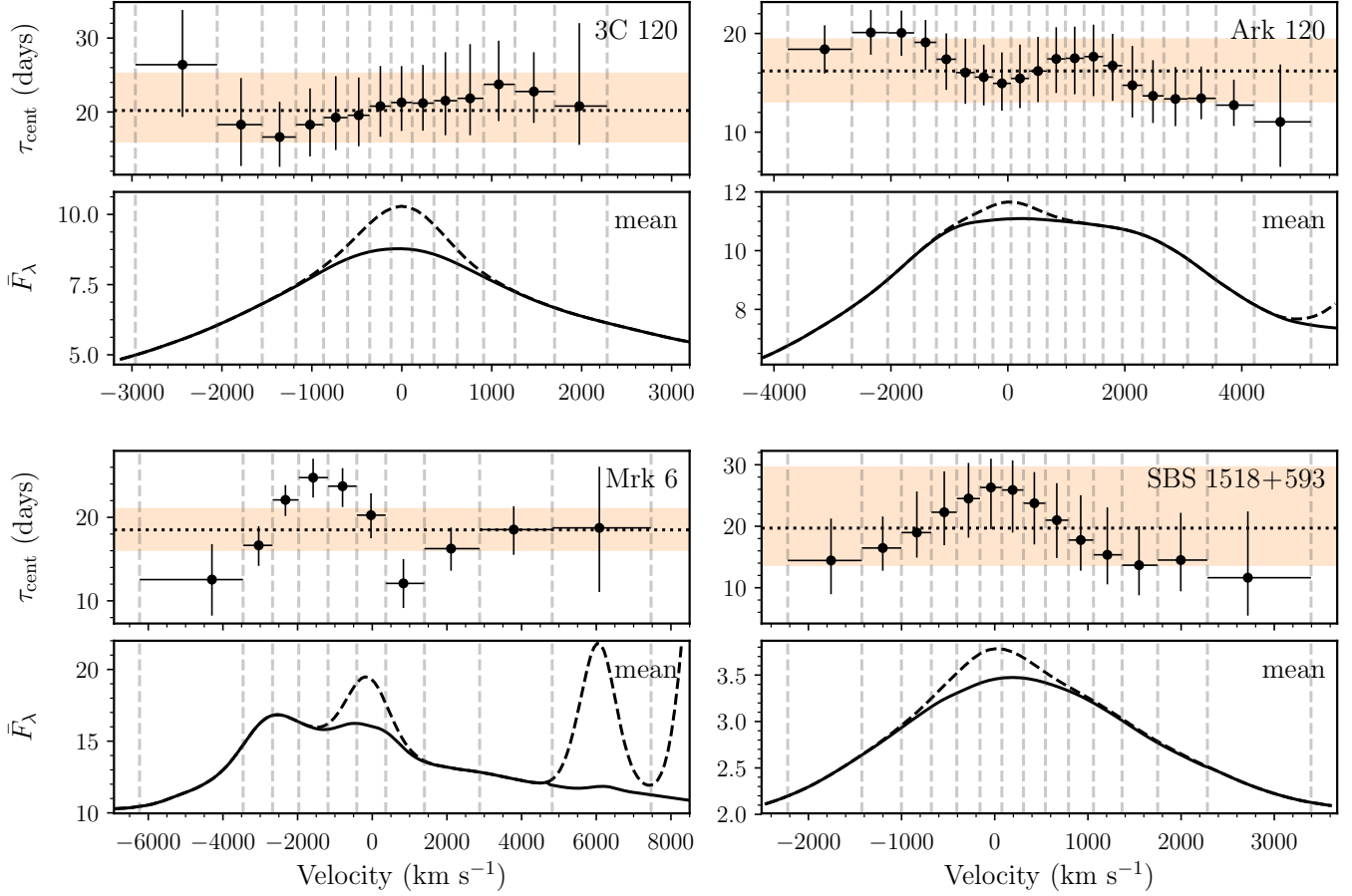


**Figure 6.** Rest-frame velocity-resolved time lags and the corresponding mean spectra. The upper panel in each plot shows the centroid lags at different velocities, and the lower panel is the mean spectrum in unit of  $10^{-15} \text{ erg s}^{-1} \text{ cm}^{-2} \text{ \AA}^{-1}$ . The name of the object is marked in the upper-right corner of each plot. The vertical dashed lines are the edges of velocity bins. The horizontal dotted lines and the orange color are the average time lags and the uncertainties in Table 4. The black dashed lines in the lower panels are the narrow emission lines.

to avoid the potential influence from the strong [O III]. For the other 3 objects, the number of bins and the bluest and reddest velocity limits are the same as the rms-based results (Figure 4). In general, the results are almost the same as the velocity-resolved lags in Section 4.4, which means the velocity-resolved analysis in this work is robust.

## REFERENCES

- Bahcall, J. N., Kozlovsky, B.-Z., & Salpeter, E. E. 1972, *ApJ*, 171, 467
- Baldi, R. D., Capetti, A., Robinson, A., Laor, A., & Behar, E. 2016, *MNRAS*, 458, L69
- Bañados, E., Venemans, B. P., Mazzucchelli, C., et al. 2018, *Nature*, 553, 473
- Barth, A. J., Bennert, V. N., Canalizo, G., et al. 2015, *ApJS*, 217, 26
- Barth, A. J., Pancoast, A., Bennert, V. N., et al. 2013, *ApJ*, 769, 128
- Barth, A. J., Pancoast, A., Thorman, S. J., et al. 2011, *ApJ*, 743, 4
- Baskin, A., & Laor, A. 2018, *MNRAS*, 474, 1970
- Begelman, M. C., Blandford, R. D., & Rees, M. J. 1980, *Nature*, 287, 307
- Bentz, M. C., Denney, K. D., Grier, C. J., et al. 2013, *ApJ*, 767, 149
- Bentz, M. C., Walsh, J. L., Barth, A. J., et al. 2008, *ApJ*, 689, L21
- Bentz, M. C., Walsh, J. L., Barth, A. J., et al. 2009, *ApJ*, 705, 199
- Bentz, M. C., Walsh, J. L., Barth, A. J., et al. 2010, *ApJ*, 716, 993
- Blandford, R. D., & McKee, C. F. 1982, *ApJ*, 255, 419
- Bon, E., Jovanović, P., Marziani, P., et al. 2012, *ApJ*, 759, 118
- Bon, E., Zucker, S., Netzer, H., et al. 2016, *ApJS*, 225, 29
- Boroson, T. A., & Green, R. F. 1992, *ApJS*, 80, 109
- Boroson, T. A., & Lauer, T. R. 2009, *Nature*, 458, 53
- Brotherton, M. S. 1996, *ApJS*, 102, 1
- Cackett, E. M., & Horne, K. 2006, *MNRAS*, 365, 1180
- Czerny, B., & Hryniewicz, K. 2011, *A&A*, 525, L8

- Decarli, R., Dotti, M., Fumagalli, M., et al. 2013, *MNRAS*, 433, 1492
- Denney, K. D., Peterson, B. M., Pogge, R. W., et al. 2009, *ApJ*, 704, L80
- Denney, K. D., Peterson, B. M., Pogge, R. W., et al. 2010, *ApJ*, 721, 715
- Dietrich, M., Peterson, B. M., Grier, C. J., et al. 2012, *ApJ*, 757, 53
- Doroshenko, V. T., Sergeev, S. G., & Pronik, V. I. 2008, *Astronomy Reports*, 52, 442
- Doroshenko, V. T., Sergeev, S. G., Klimanov, S. A., Pronik, V. I., & Efimov, Y. S. 2012, *MNRAS*, 426, 416
- De Robertis, M. 1985, *ApJ*, 289, 67
- Doroshenko, V. T., & Sergeev, S. G. 2003, *A&A*, 405, 909
- Du, P., Hu, C., Lu, K.-X., et al. 2014, *ApJ*, 782, 45
- Du, P., Hu, C., Lu, K.-X., et al. 2015, *ApJ*, 806, 22
- Du, P., Lu, K.-X., Hu, C., et al. 2016a, *ApJ*, 820, 27
- Du, P., Lu, K.-X., Zhang, Z.-X., et al. 2016b, *ApJ*, 825, 126
- Du, P., Wang, J.-M., & Zhang, Z.-X. 2017, *ApJL*, 840, L6
- Du, P., Zhang, Z.-X., Wang, K., et al. 2018, *ApJ*, 856, 6
- Elvis, M. 2017, *ApJ*, 847, 56
- Eracleous, M., & Halpern, J. P. 1993, *ApJ*, 409, 584
- Eracleous, M., & Halpern, J. P. 1994, *ApJS*, 90, 1
- Eracleous, M., Halpern, J. P., M. Gilbert, A., Newman, J. A., & Filippenko, A. V. 1997, *ApJ*, 490, 216
- Eracleous, M., Boroson, T. A., Halpern, J. P., & Liu, J. 2012, *ApJS*, 201, 23
- Fausnaugh, M. M. 2017, *PASP*, 129, 024007
- Fausnaugh, M. M., Grier, C. J., Bentz, M. C., et al. 2017, *ApJ*, 840, 97
- Findlay, J. R., Kobulnicky, H. A., Weger, J. S., et al. 2016, *PASP*, 128, 115003
- Francis, P. J., & Koratkar, A. 1995, *MNRAS*, 274, 504
- Gaskell, C. M. 2009, *NewAR*, 53, 140
- Gaskell, C. M. 1996, *ApJL*, 464, L107
- Gaskell, C. M., & Harrington, P. Z. 2018, *MNRAS*, 478, 1660
- Gaskell, C. M., & Peterson, B. M. 1987, *ApJS*, 65, 1
- Gaskell, C. M., & Sparke, L. S. 1986, *ApJ*, 305, 175
- Graham, M. J., Djorgovski, S. G., Stern, D., et al. 2015, *Nature*, 518, 74
- Grier, C. J., Martini, P., Watson, L. C., et al. 2013a, *ApJ*, 773, 90
- Grier, C. J., Peterson, B. M., Horne, K., et al. 2013b, *ApJ*, 764, 47
- Grier, C. J., Peterson, B. M., Pogge, R. W., et al. 2012, *ApJ*, 755, 60
- Grier, C. J., Pancoast, A., Barth, A. J., et al. 2017a, *ApJ*, 849, 146
- Grier, C. J., Trump, J. R., Shen, Y., et al. 2017b, *ApJ*, 851, 21
- Goad, M. R., & Korista, K. T. 2015, *MNRAS*, 453, 3662
- Ho, L. C., & Kim, M. 2014, *ApJ*, 789, 17
- Horne, K. 1994, in *ASP Conf. Ser. 69, Reverberation Mapping of the Broad-Line Region in Active Galactic Nuclei*, ed. P. M. Gondhalekar, K. Horne, & B. M. Peterson (San Francisco: ASP), 23
- Horne, K., Peterson, B. M., Collier, S. J., & Netzer, H. 2004, *PASP*, 116, 465
- Hu, C., Du, P., Lu, K.-X., et al. 2015, *ApJ*, 804, 138
- Hu, C., Wang, J.-M., Ho, L. C., et al. 2008a, *ApJ*, 687, 78
- Hu, C., Wang, J.-M., Ho, L. C., et al. 2008b, *ApJL*, 683, L115
- Jovanović, P., Popović, L. Č., Stalevski, M., & Shapovalova, A. I. 2010, *ApJ*, 718, 168
- Kaspi, S., Brandt, W. N., Maoz, D., et al. 2007, *ApJ*, 659, 997
- Kaspi, S., Smith, P. S., Netzer, H., et al. 2000, *ApJ*, 533, 631
- Kewley, L. J., Groves, B., Kauffmann, G., & Heckman, T. 2006, *MNRAS*, 372, 961
- Khachikian, E. Y., & Weedman, D. W. 1971, *ApJL*, 164, L109
- Kharb, P., O’Dea, C. P., Baum, S. A., et al. 2014, *MNRAS*, 440, 2976
- Kochanek, C. S., Shappee, B. J., Stanek, K. Z., et al. 2017, *PASP*, 129, 104502
- Kollatschny, W., Ulbrich, K., Zetzl, M., Kaspi, S., & Haas, M. 2014, *A&A*, 566, A106
- Korista, K. T., & Goad, M. R. 2004, *ApJ*, 606, 749
- Kukula, M. J., Holloway, A. J., Pedlar, A., et al. 1996, *MNRAS*, 280, 1283
- Li, Y.-R., Wang, J.-M., Ho, L. C., et al. 2016, *ApJ*, 822, 4
- Li, Y.-R., Wang, J.-M., Zhang, Z.-X., et al. 2017, *arXiv:1705.07781*
- Liu, T., Gezari, S., & Miller, M. C. 2018, *ApJL*, 859, L12
- Marziani, P., Sulentic, J. W., Zamanov, R., et al. 2003, *ApJS*, 145, 199
- Mortlock, D. J., Warren, S. J., Venemans, B. P., et al. 2011, *Nature*, 474, 616
- Murray, N., & Chiang, J. 1997, *ApJ*, 474, 91
- Nguyen, K., & Bogdanović, T. 2016, *ApJ*, 828, 68
- Onken, C. A., Ferrarese, L., Merritt, D., et al. 2004, *ApJ*, 615, 645
- Osterbrock, D. E., & Mathews, W. G. 1986, *ARA&A*, 24, 171
- Park, D., Kelly, B. C., Woo, J.-H., & Treu, T. 2012, *ApJS*, 203, 6
- Pancoast, A., Brewer, B. J., & Treu, T. 2011, *ApJ*, 730, 139
- Pancoast, A., Brewer, B. J., Treu, T., et al. 2012, *ApJ*, 754, 49
- Pancoast, A., Brewer, B. J., Treu, T., et al. 2014, *MNRAS*, 445, 3073
- Peterson, B. M. 1997, *An introduction to active galactic nuclei*, Publisher: Cambridge, New York Cambridge University Press, 1997 Physical description xvi, 238 p. ISBN 0521473489
- Peterson, B. M., Ali, B., Horne, K., et al. 1993, *PASP*, 105, 247
- Peterson, B. M., Berlind, P., Bertram, R., et al. 2002, *ApJ*, 581, 197
- Peterson, B. M., Denney, K. D., De Rosa, G., et al. 2013, *ApJ*, 779, 109
- Peterson, B. M., Ferrarese, L., Gilbert, K. M., et al. 2004, *ApJ*, 613, 682
- Peterson, B. M., & Wandel, A. 1999, *ApJL*, 521, L95
- Peterson, B. M., Wanders, I., Bertram, R., et al. 1998, *ApJ*, 501, 82
- Pflueger, B. J., Nguyen, K., Bogdanović, T., et al. 2018, *ApJ*, 861, 59

- Press, W. H., Teukolsky, S. A., Vetterling, W. T., & Flannery, B. P. 1992, Cambridge: University Press, —c1992, 2nd ed.,
- Popovic, L. C., Mediavilla, E. G., & Pavlovic, R. 2000, *Serbian Astronomical Journal*, 162, 1
- Rafter, S. E., Kaspi, S., Behar, E., Kollatschny, W., & Zetzl, M. 2011, *ApJ*, 741, 66
- Rafter, S. E., Kaspi, S., Chelouche, D., et al. 2013, *ApJ*, 773, 24
- Runnoe, J. C., Eracleous, M., Pennell, A., et al. 2017, *MNRAS*, 468, 1683
- Savić, D., Goosmann, R., Popović, L. Č., Marin, F., & Afanasiev, V. L. 2018, *A&A*, 614, A120
- Schmidt, M. 1963, *Nature*, 197, 1040
- Schneider, D. P., Richards, G. T., Hall, P. B., et al. 2010, *AJ*, 139, 2360
- Sergeev, S. G., Nazarov, S. V., & Borman, G. A. 2017, *MNRAS*, 465, 1898
- Sergeev, S. G., Pronik, V. I., Sergeeva, E. A., & Malkov, Y. F. 1999, *ApJS*, 121, 159
- Sesana, A., Vecchio, A., & Colacino, C. N. 2008, *MNRAS*, 390, 192
- Shapovalova, A. I., Popović, L. Č., Burenkov, A. N., et al. 2010, *A&A*, 517, A42
- Shappee, B. J., Prieto, J. L., Grupe, D., et al. 2014, *ApJ*, 788, 48
- Shen, Y., Brandt, W. N., Richards, G. T., et al. 2016a, *ApJ*, 831, 7
- Shen, Y., Horne, K., Grier, C. J., et al. 2016b, *ApJ*, 818, 30
- Shen, Y., & Loeb, A. 2010, *ApJ*, 725, 249
- Shen, Y., Liu, X., Loeb, A., & Tremaine, S. 2013, *ApJ*, 775, 49
- Shen, Y., Richards, G. T., Strauss, M. A., et al. 2011, *ApJS*, 194, 45
- Skielboe, A., Pancoast, A., Treu, T., et al. 2015, *MNRAS*, 454, 144
- Smith, J. E., Robinson, A., Young, S., Axon, D. J., & Corbett, E. A. 2005, *MNRAS*, 359, 846
- Stern, J., & Laor, A. 2013, *MNRAS*, 431, 836
- Stirpe, G. M. 1990, *A&AS*, 85, 1049
- Storchi-Bergmann, T., Schimoia, J. S., Peterson, B. M., et al. 2017, *ApJ*, 835, 236
- Sulentic, J. W., Marziani, P., & Dultzin-Hacyan, D. 2000, *ARA&A*, 38, 521
- van Groningen, E., & Wanders, I. 1992, *PASP*, 104, 700
- Vanden Berk, D. E., Richards, G. T., Bauer, A., et al. 2001, *AJ*, 122, 549
- Volonteri, M., & Madau, P. 2008, *ApJL*, 687, L57
- Wandel, A., Peterson, B. M., & Malkan, M. A. 1999, *ApJ*, 526, 579
- Wang, J.-M., Songsheng, Y.-Y., Li, Y.-R., & Zhe, Y. 2018, *ApJ*, in press, arXiv:1806.06487
- Wang, J.-M., Du, P., Brotherton, M. S., et al. 2017a, *Nature Astronomy*, 1, 775
- Wang, L., Greene, J., Ju, W. et al. 2017b, *ApJ*, 834, 129
- Wang, J.-M., Du, P., Hu, C., et al. 2014, *ApJ*, 793, 108
- Welsh, W. F., & Horne, K. 1991, *ApJ*, 379, 586
- Whittle, M. 1992, *ApJS*, 79, 49
- Wills, B. J., & Browne, I. W. A. 1986, *ApJ*, 302, 56
- Wills, B. J., Brandt, W. N., & Laor, A. 1999, *ApJL*, 520, L91
- Woo, J.-H., Treu, T., Barth, A. J., et al. 2010, *ApJ*, 716, 269
- Woo, J.-H., Yoon, Y., Park, S., Park, D., & Kim, S. C. 2015, *ApJ*, 801, 38